Rewired m6A methylation of promoter antisense RNAs in Alzheimer's disease regulates global gene transcription in the 3D nucleome

Benxia Hu[1,#], Yuqiang Shi[1,#], Feng Xiong[1], Yi-Ting Chen[1,2], Xiaoyu Zhu[1], Elisa Carrillo [1], Xingzhao Wen[3,4], Nathan Drolet[1], Chetan Rajpurohit[5], Xiangmin Xu[6,7], Dung-Fang Lee[2,8], Claudio Soto[2,9], Sheng Zhong[3,4], Vasanthi Jayaraman [1,2], Hui Zheng[5], Wenbo Li[1,2 *]

[1] Department of Biochemistry and Molecular Biology, McGovern Medical School, University of Texas Health Science Center, Houston, TX, USA.

[2] The University of Texas MD Anderson Cancer Center and UTHealth Houston Graduate School of Biomedical Sciences, Houston, TX, USA.

[3] Program in Bioinformatics and Systems Biology, University of California San Diego, La Jolla, CA, USA.

[4] Shu Chien-Gene Lay Department of Bioengineering, University of California San Diego, La Jolla, CA, USA.

[5] Huffington Center on Aging, Baylor College of Medicine, Houston, Texas, USA.

[6] Department of Anatomy and Neurobiology, School of Medicine, University of California, Irvine, CA, USA.

[7] Center for Neural Circuit Mapping (CNCM), University of California, Irvine, CA, USA.

[8] Department of Integrative Biology and Pharmacology, McGovern Medical School, The University of Texas Health Science Center at Houston, Houston, TX, USA.

[9] Department of Neurology, McGovern Medical School, University of Texas Health Science Center, Houston, TX, USA.

[#] Contributed equally.

[*] Corresponding author, Wenbo.li@uth.tmc.edu.

Abstract

N^6-methyladenosine (m6A) is the most prevalent internal RNA modification that can impact mRNA expression post-transcriptionally. Recent progress indicates that m6A also acts on nuclear or chromatin-associated RNAs to impact transcriptional and epigenetic processes. However, the landscapes and functional roles of m6A in human brains and neurodegenerative diseases, including Alzheimer's disease (AD), have been under-explored. Here, we examined RNA m6A methylome using total RNA-seq and meRIP-seq in middle frontal cortex tissues of post-mortem human brains from individuals with AD and age-matched counterparts. Our results revealed AD-associated alteration of m6A methylation on both mRNAs and various noncoding RNAs. Notably, a series of promoter antisense RNAs (paRNAs) displayed cell-type-specific expression and changes in AD, including one produced adjacent to the *MAPT* locus that encodes the Tau protein. We found that *MAPT-paRNA* is enriched in neurons, and m6A positively controls its expression. In iPSC-derived human excitatory neurons, *MAPT-paRNA* promotes expression of hundreds of genes related to neuronal and synaptic functions, including a key AD resilience gene *MEF2C*, and plays a neuroprotective role against excitotoxicity. By examining RNA-DNA interactome in the three-dimensional (3D) nuclei of human brains, we demonstrated that brain paRNAs can interact with both *cis*- and *trans*-chromosomal target genes to impact their transcription. These data together reveal previously unexplored landscapes and functions of noncoding RNAs and m6A methylome in brain gene regulation, neuronal survival and AD pathogenesis.

Introduction

Alzheimer's disease (AD) is the most common cause of dementia (60–70% of all cases), and affects 5% of the population over 60 years (or approximately 1% of the total population)[1]. AD is pathologically characterized by massive neuronal loss, the presence of amyloid-beta (Aβ) plaques, and Tau neurofibrillary tangles (NFTs) in the brain[2,3]. Despite extensive studies of AD, there are still limited therapeutic options that can effectively treat this devastating disease. Identifying new molecular players in AD pathogenesis is important to offer further insights and potential targets for combating this disease.

In the past decade, studies of RNA chemical modifications have founded a field that is referred to as "epitranscriptomics"[4,5]. Among these RNA modifications, N^6-methyladenosine (m6A) is the most abundant internal RNA methylation in mammalian cells, and it can impact mRNA stability, trafficking, and translation[4,5]. Analogous to the mechanism of epigenetics, biological functions of m6A are considered to be mediated by specific proteins that write, read, and erase this mark, which are referred to as m6A writers (e.g., METTL3), readers (e.g., YTH proteins), and erasers (e.g., FTO and ALKBH5), respectively[4,5]. In addition to post-transcriptional roles on mRNAs, m6A methylation is increasingly realized to bear transcriptional roles by modifying nuclear or chromatin-associated RNAs to control gene transcription via functionally cross-talking to epigenetic processes[6-10]. Examples include m6A regulation of *Xist* lncRNA[8,11], retrotransposon RNAs[10,12-14], or enhancer RNAs[7,15]. These results have provided a new perspective to study the roles of m6A in gene regulation in development and diseases, which encompasses both transcriptional and post-transcriptional processes. Interestingly, m6A methylation seems to play unique functions in the brain. For example, in both mice and human brains, m6A landscapes display a pattern distinctive from other tissues[16]. In murine models, conditional depletion of genes encoding a component of the m6A methyltransferase complex, Mettl14, or a cytoplasmic m6A reader protein, Ythdf1, severely affected neurogenesis and cognitive functions[17,18]. However, despite efforts[19], the landscapes and functional roles of m6A or other epitranscriptomic modifications in human brains and AD remain minimally explored.

Regulatory long noncoding RNAs (lncRNAs) are pervasively produced in the human genome[20,21]. A large fraction of these transcripts originate from divergent transcription at

80 promoters of active protein-coding genes (>60% in human ESCs[22]), which are interchangeably
81 referred to as promoter antisense RNAs (paRNAs) or PTOMPTs[23-27]. Some studies reported that
82 paRNAs can regulate the expression of mRNAs divergently produced from the same
83 promoters[27,28]. Actually, deregulation of lncRNAs has been long observed in AD[29-31]. An early
84 example is an antisense RNA produced within the *BACE1* gene locus that was proposed to
85 regulate *BACE1* expression to impact AD disease progression[32]. High resolution transcriptomes
86 in AD brains have now permitted rapid discovery of enormous ncRNAs[30,31]. A recent work
87 suggested that AD-associated natural antisense transcripts (NAT), some of which are paRNAs,
88 can play roles in the translational control of crucial disease proteins including MAPT/Tau to
89 impact AD pathogenesis[33]. However, another study reported inconsistent results[34]. These studies
90 together indicated that the roles of lncRNAs are still under-studied in human AD brains, and
91 their mechanisms of action are poorly understood.
92
93 Here, we characterized RNA m6A methylome from individuals diagnosed with AD and from
94 cognitively normal age-matched individuals. We uncovered a large number of m6A-modified
95 RNAs in the human brain, including both mRNAs and ncRNAs, many of which were previously
96 unannotated. RNA m6A methylome in AD brains displays alteration as compared to controls,
97 and there is positive correlation between its signals and expression levels of mRNA and
98 ncRNAs. Subsequently, we focused on paRNAs and used induced pluripotent stem cell (iPSC)-
99 derived human excitatory neurons (i3Neurons) to functionally investigate regulatory roles of an
100 m6A-modified *MAPT-paRNA* transcribed next to *MAPT*, a key AD-associated disease locus. Our
101 data revealed that *MAPT-paRNA* shows neuron-preferred expression and is upregulated in AD. It
102 promotes the expression of many neuronal and synaptic genes via navigating the three-
103 dimensional (3D) genome organization, which is required for neuronal survival under excitotoxic
104 conditions. This work unraveled previously unexplored landscapes and the role of chemical
105 modification on AD-associated ncRNAs, linking epitranscriptome to gene transcriptional control
106 in the 3D genome and AD pathogenesis.
107
108 **Results**
109 **The transcriptome and m6A epitranscriptome of human AD brains on coding and**
110 **noncoding RNAs**

111 From a cohort of individuals diagnosed with sporadic AD (n = 6; mean age = 66) and from
112 cognitively normal age-matched counterparts (n = 6; mean age = 65, hereafter referred to as
113 Normal), we collected the middle frontal cortex tissue (mFC), a region pathologically affected in
114 AD[35]. Subsequent to autopsy, neuropathologic examination revealed high levels of
115 phosphorylated Tau neurofibrillary tangles and amyloid-β burden (**Supplementary Table 1**).
116 We analyzed the transcriptome by strand-specific ribo-depleted total RNA-seq, with the aim of
117 examining both mRNAs and various ncRNAs. RNA m6A methylome was examined by m6A
118 antibody-based immunoprecipitation (MeRIP-seq) (**see methods**). A summary of our sequencing
119 datasets can be found in **Supplementary Table 2**.
120
121 Analysis of total RNA-seq data identified 416 and 519 genes significantly upregulated and
122 downregulated in AD as compared to Normal groups, respectively (**Supplementary Fig. 1A**,
123 gene lists in **Supplementary Table 3**). These changes are consistent with a previous study that
124 conducted total RNA-seq in the lateral temporal lobe (LTL) region of AD/Normal human
125 brains[36] (**Supplementary Fig. 1B,C**). Gene Ontology (GO) analysis of differentially expressed
126 genes (DEGs) showed that AD-upregulated genes are related to development, while the AD-
127 downregulated genes are enriched in neuronal/synaptic functions (**Supplementary Fig. 1D,E,**
128 and **Supplementary Table 4**). This is in accord with the knowledge that neuronal/synaptic genes
129 are reduced in AD[37]. This also suggests that tissue-level gene deregulation that we found here
130 largely reflects changes in neurons[38]. Several representative examples of deregulated genes are
131 shown in **Supplementary Fig. 1F**. *YAP1*, a gene encoding a key transcription regulator, was
132 induced in AD, whereas AD-downregulated genes are exemplified by neuronal transcriptional
133 factor gene *NEUROD6* and those encoding glutamate decarboxylases essential for inhibitory
134 neurotransmitter gamma-aminobutyric acid (GABA) synthesis, e.g., *GAD1*/*GAD2*
135 (**Supplementary Fig. 1F**).

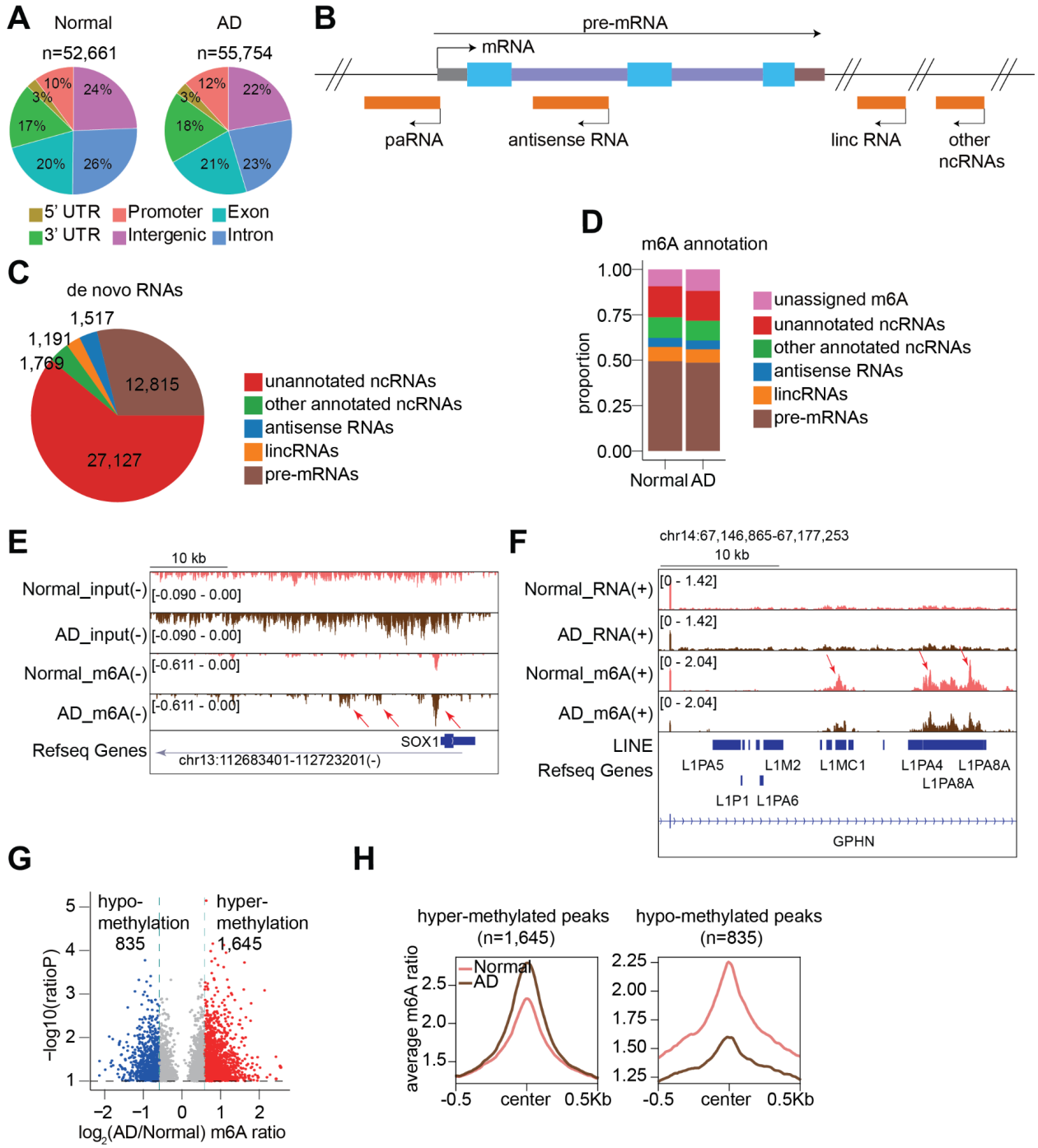

Figure 1. m6A methylome on coding and noncoding RNAs in the mFC regions of human brains. **A**. Piecharts showing the m6A peak distribution based on genomic locations in post-mortem human mFC tissues from Normal and AD donors, respectively. **B.** A model illustrating major categories of *de novo* identified transcripts, including pre-mRNAs and ncRNAs. **C**. A piechart showing the numbers of transcripts identified by the de novo calling. **D**. A barplot showing the assignment of m6A peaks to various *de novo* called transcripts. **E.** Genome browser tracks showing an example of ncRNA (a promoter antisense RNA from the *SOX1* locus) having m6A peaks in human Normal and AD brains. Input and m6A represent the average signals of RNA-seq and meRIP-seq datasets in this work, respectively. The arrows indicate m6A peaks. **F.** Similar to E, example tracks showing intronic L1 elements overlap m6A peaks in the intron of *GPHN* gene. (+) and (-) indicate the Watson and Crick strands, respectively. **G.** A volcano plot showing differential m6A peaks between Normal and AD brains. Red and blue dots

147 represent hyper- and hypo-methylated m6A sites in AD. **H**. Metaplots showing the aggregated m6A ratios of hyper-
148 and hypo-methylated m6A sites.
149

150 To examine the changes of RNA m6A methylome in AD versus Normal brains, we called strand-
151 specific m6A peaks on total RNA-Seq/MeRIP-seq datasets using MACS3[39,40], and identified
152 approximately 52,661 and 55,754 m6A peaks in Normal and AD mFC tissues, respectively
153 (**Supplementary Table 5**). A majority of peaks locate in the non-protein-coding portions of the
154 genome, i.e., around 60% were in intergenic regions, introns or promoter upstream regions (-2kb
155 to transcription start sites) (**Fig. 1A**). The remaining peaks overlapped with protein-coding
156 mRNA sequences (CDSs), and 5' or 3′ untranslated regions (UTRs) (**Fig. 1A**). This is consistent
157 with the higher sensitivity of ribo-depletion strategy in RNA-seq to detect various ncRNAs. We
158 compared the features of m6A peaks in Normal and AD conditions, and found them to be overall
159 similar: they enrich the canonical RRACH motif, bearing comparable peak length (Normal:
160 236bp v.s. AD: 227bp) and average GC contents (0.47 v.s. 0.45) (**Supplementary Fig. 2A,B,C**).
161 The genomic distribution of m6A signals is quite similar between RNAs from Normal and AD
162 brains, too (**Supplementary Fig. 2D**). These results indicate that AD elicits a quantitative
163 rewiring of the RNA m6A landscape in the human brain, at least in the mFC region.
164

165 A large number of m6A peaks locating in the noncoding regions is consistent with recent work
166 about m6A on regulatory ncRNAs[7,8,12,15,41]. Annotation of m6A peaks using genomic locations is
167 not sufficient to precisely associate them to specific noncoding RNA transcripts (**Fig. 1A,B**). We
168 therefore need to first define a complete catalog of transcripts and their genomic coordinates in
169 the human brain by a *de novo* transcript calling method based on Hidden Markov Model (HMM)
170 [42,43]. Of the *de novo* identified transcripts, 12,815 overlap protein-coding genes and are thus
171 defined as pre-mRNAs in this work (**Fig. 1B,C**). There are 31,604 ncRNA transcripts in the
172 human brain (**Fig. 1C**), including 27,127 previously unannotated RNAs in the human
173 transcriptome. Of the remaining, 1,191 overlap annotated lncRNAs, 1,517 overlap annotated
174 antisense RNAs, and 1,769 overlap other annotated RNAs (snoRNAs, snRNAs, pseudo genes) in
175 gencode v19 (**Fig. 1C**). Approximately 90% of all m6A peaks can be assigned to these various
176 *de novo* identified RNAs (**Supplementary Fig. 2E,** and **Fig. 1D**). The ~10% unassigned peaks
177 are largely due to the fact that some RNAs are not identified as independent transcripts by the *de*
178 *novo* calling algorithm and thus m6A peaks on them are not assigned. As an example, of the

179 27,127 previously unannotated transcripts (**Fig. 1C,D**), an antisense RNA generated from the
180 *SOX1* gene promoter shows prominent m6A peaks (**Fig. 1E**). About 50% of m6A peaks were
181 assigned to the sense strand of pre-mRNAs, including exons, introns, 5'UTR and 3'UTR (**Fig.**
182 **1D,F**). Among these, interestingly, over ten-thousand peaks appear in introns and often overlap
183 transposable elements, in particular, intronic L1 elements (**Fig. 1F,** and **Supplementary Fig.**
184 **2F,G,H**). This is reminiscent of our previous work showing that many intronic L1 RNAs bear
185 high m6A methylation and play roles in gene transcriptional control[12]. Collectively, at the
186 transcriptome level, 60-70% of all m6A peaks are located in ncRNAs or introns as opposed to
187 mRNA regions (UTRs and exons), and the distribution pattern is largely similar in AD versus
188 Normal (**Supplementary Fig. 2H**). These results provided a comprehensive m6A RNA
189 methylome on mRNAs and ncRNAs in human Normal and AD brains, serving as a foundation to
190 study the functions of these m6A signals in gene expression regulation and AD biology.
191
192 **The alteration of m6A epitranscriptome in the human AD brains**
193 By calculating differential m6A methylation (**see methods**), we identified 835 and 1,645
194 differential m6A peaks (DMPs) showing hypo- and hyper-m6A-methylation in AD, respectively
195 (**Fig. 1G**). Here we defined m6A methylation levels as m6A ratios, the signal division between
196 meRIP-seq and RNA-seq in each peak. The changes in m6A ratios at the differential peaks can
197 be seen by meta-analysis (**Fig. 1H**), and the motifs in these regions remain canonical RRACH
198 (**Supplementary Fig. 3A**). A breakdown shows that DMPs overall occurred proportionally to
199 the total peak distribution, with about 40% of DMPs on pre-mRNAs (including exons, UTRs and
200 introns) and the other ~60% of DMPs are observed to be from ncRNAs (**Fig. 1D**, and
201 **Supplementary Fig. 3B**).
202
203 Previous m6A studies have shown correlation between changes of m6A and mRNA expression
204 levels[4,44]. We examined their correlation in AD brains by examining mRNAs bearing DMPs on
205 their exons or UTRs. By cumulative fraction analysis, we observed a positive correlation
206 between the two, i.e., m6A hyper-methylation is associated with mRNA expression increase in
207 AD, whereas hypo-methylation is associated with decrease (**Supplementary Fig. 3C,D**).
208 Interestingly, GO enrichment analyses of genes whose mRNAs display hyper-methylation show
209 terms related to transcriptional activities, whereas gene mRNAs with hypo-methylated peaks are

210 more relevant to synapse regulation (**Supplementary Fig. 3E,F**). Because of the known
211 expression reduction of synapse related genes in AD[37], this result suggests that hypo-methylation
212 of their mRNAs is associated with expression reduction during AD pathogenesis. We showed
213 two representative examples of m6A peaks in the 3'UTR regions that were hyper- or hypo-
214 methylated in AD compared to Normal, which correlates with their respective mRNA expression
215 changes (**Supplementary Fig. 3G,H**). We conducted similar analysis for ncRNAs, and observed
216 that m6A changes are also positively correlated with ncRNA expression alteration in AD, i.e.,
217 hyper-methylation is associated with ncRNA expression increase, whereas hypo-methylation
218 with decrease (**Supplementary Fig. 4A,B**). We show two representative examples of ncRNA
219 regions that were increased or decreased in AD compared to Normal, respectively
220 (**Supplementary Fig. 4C,D**).
221
222 **Identification and alteration of promoter antisense RNAs in AD brains**
223 We sought to focus on previously under-studied ncRNAs and their m6A modification in AD.
224 Visual inspection revealed a large number of paRNAs that display m6A peaks, which
225 interestingly include many produced from important neuronal and synaptic gene loci. For
226 example, an m6A-marked paRNA spanning ~18kb is generated from the *GRIN2A* locus (**Fig.
227 2A**), which codes for an important neurotransmitter receptor Glutamate Ionotropic Receptor
228 NMDA Type Subunit 2A. Similarly, another m6A-marked paRNA is produced antisense to the
229 promoter of *MAPT*, one of the most significant AD-associated loci as it encodes the Tau protein
230 (**Fig. 2B**). Importantly, functions of paRNAs have been minimally studied or understood in brain
231 gene regulation and AD biology. *De novo* calling identified 3,038 paRNAs in mFC brain regions
232 and about 37-39% of them display a m6A peak in either Normal or AD brains (**Supplementary
233 Fig. 5A**). GO term analysis showed that genes neighboring m6A-marked paRNAs are associated
234 with neuronal and synapse functions, which are deregulated processes in AD (**Fig. 2C,D**). In
235 comparison, mRNAs with m6A do not show such association (**Supplementary Fig. 5B**),
236 suggesting that m6A-marked paRNAs in mFCs may have specific relevance to neuronal/synapse
237 biology. Because we observed some paRNAs with exceptional length, we utilized public
238 nanopore long-read direct RNA-seq as an orthogonal method to validate paRNA existence and
239 length (from dorsolateral prefrontal cortex (DLPFC) brain region by the Rush Alzheimer's
240 Disease Study). Defining the lengths of paRNAs is important to assign m6A peaks to these

241 paRNA transcripts, because the peaks can sometimes be located >10kb away from the TTSs, as
242 exemplified in **Fig. 2A,B** (and other examples see below). Despite the low coverage and its
243 utilization of polyA capture, long-reads RNA-seq data detected about 25% of paRNAs seen by
244 our *de novo* calling of total RNA-seq data, and the length estimation is highly accurate
245 (**Supplementary Fig. 5C,D**). Globally, paRNA expression levels appeared comparable in
246 Normal and AD mFCs, but those with m6A modifications are expressed higher than those
247 without (**Supplementary Fig. 5E,F**), suggesting a positive influence of m6A methylation on
248 paRNAs expression.
249
250 Differential analysis of paRNAs revealed 88 upregulated and 99 downregulated paRNAs in AD
251 mFC regions (**Fig. 2E,** and **Supplementary Table 6**). These changes are also recapitulated by
252 total RNA-seq data from Normal/AD brains by Nativio et al.[36] (from LTL brain region, **Fig. 2F**).
253 paRNAs altered in AD versus Normal brains are distinct from those changed in normal aging
254 (old versus young human brains that are cognitively normal, **Fig. 2F**), suggesting potential
255 involvement of these RNAs in AD pathogenesis. Interestingly, we found that paRNAs
256 upregulated in AD are much longer than paRNAs downregulated in AD, a pattern not observed
257 for deregulated protein-coding genes (**Supplementary Fig. 5G**). Although it is currently unclear
258 what the molecular basis underlying this observation is, we speculate that there are malfunctions
259 of RNA processing in AD that deregulate paRNAs in a length-related manner. Consistent with
260 the correlation seen for mRNAs and other ncRNAs, hyper- and hypo-methylation of paRNA is
261 correlated with their expression increase and decrease in AD, respectively (**Fig. 2G,H**).

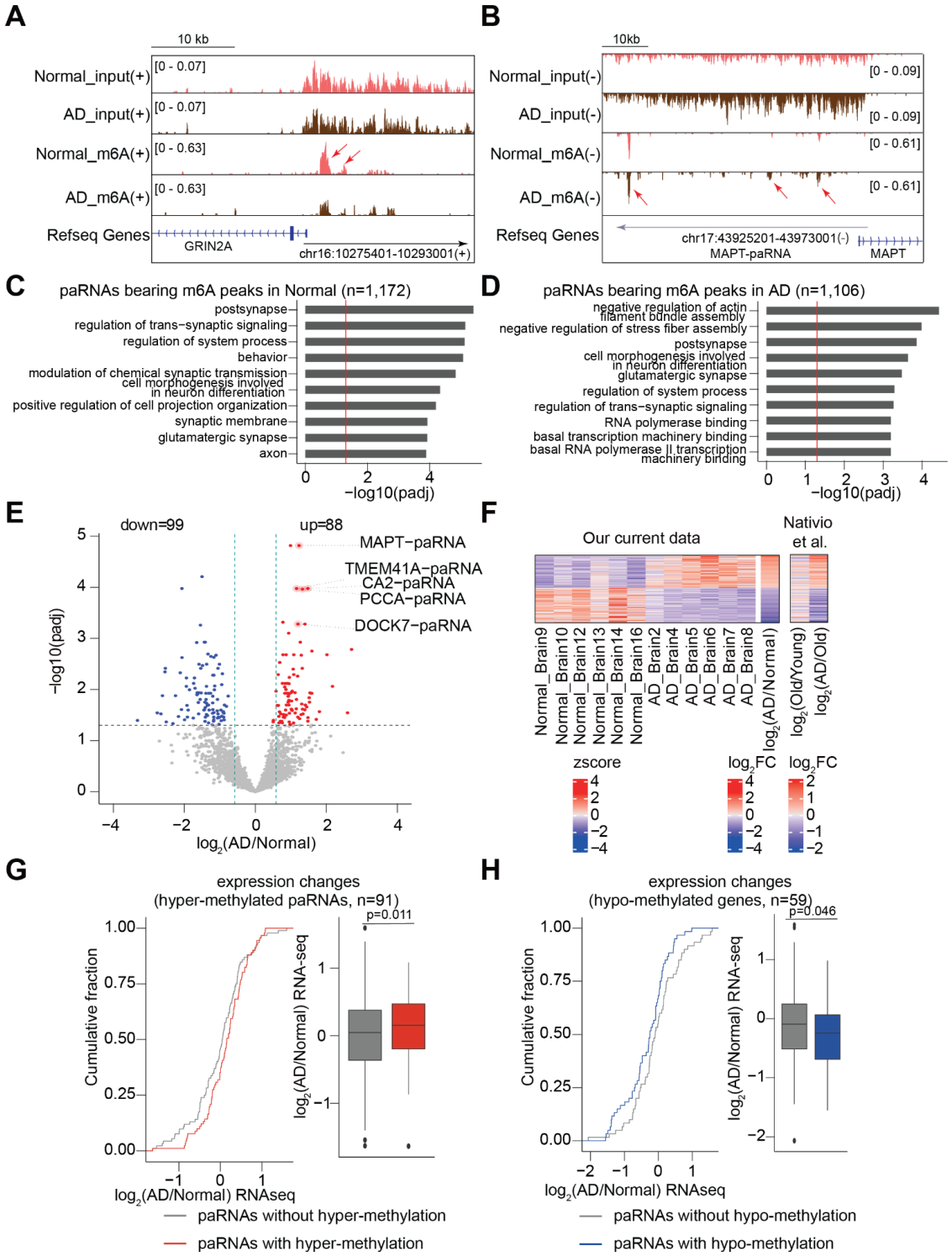

Figure 2. The m6A methylation and expression of paRNAs in Normal and AD human brains. A,B. Genome browser tracks showing the RNA-seq and m6A signals of two paRNAs (*GRIN2A-paRNA* and *MAPT-paRNA*) in the human mFC. Red arrows indicate m6A peaks. **C,D**. GO analyses for genes neighboring and sharing promoters with paRNAs. The red lines represent adjusted p values (p-adj) at 0.05. **E**. A volcano plot showing differentially expressed paRNAs between Normal and AD brains. Red and blue dots represent up-regulated and down-regulated paRNAs in AD, respectively. **F**. A heatmap showing z-score-transformed expression levels of differentially expressed paRNAs between Normal and AD brains from our samples, and from Nativio et al.[36]. **G,H.** Cumulative

distribution and boxplots of paRNA expression changes with or without hyper- and hypo-m6A. P values were calculated by a two-tailed non-parametric Wilcoxon–Mann–Whitney test. Boxplots indicate the interquartile range with the central line representing the median, and the vertical lines extending to the extreme values in the group.

paRNA deregulation in AD mouse model and other human neurodegenerative diseases

We examined if the paRNAs deregulated in human AD brains can be detected in 5xFAD mice brain, a well-characterized mouse model of AD[45]. Total RNA-seq data has been generated from the right cerebral hemisphere of 5xFAD mice brain (ID: syn21983020). There are 1,378 paRNAs produced from promoters of homologous genes in human and mice brains (hereafter referred to as common paRNAs) (**Fig. 3A**). Of these, about 6% (n=87) showed altered expression in human AD brains (**Fig. 3B**), and about 3% (n=42) were differentially expressed in the 5xFAD mouse brains versus wild-type controls. However, none of them is consistent between human and mouse AD brains (**Fig. 3B**). Because 5xFAD is mainly an amyloid model, whereas our human RNA-seq data are from patients bearing both Tau and amyloid pathologies, we examined another mouse model exhibiting both these two pathologies, the 3xTg-AD model[46]. Based on the same process done above for 5xFAD, we identified 3,934 paRNAs in 3xTg-AD mouse brains (hippocampus, data from syn22964719). Differential expression analysis identified 5 upregulated and 1 downregulated paRNAs in 3xTg-AD mice (n=18) compared to wild-type (n=18). There are no common differentially expressed paRNAs between 3xTg-AD mouse model and human AD brains (**Fig. 3C**). A similar conclusion is also drawn by comparing paRNA changes in the human brain versus those changes in the P301S mouse brains[47], a commonly used tauopathy model (**Fig. 3D**). Such a lack of similarity of paRNAs altered in human and mouse AD brains is consistent with the idea that AD mouse models cannot completely recapitulate human AD pathogenesis[48].

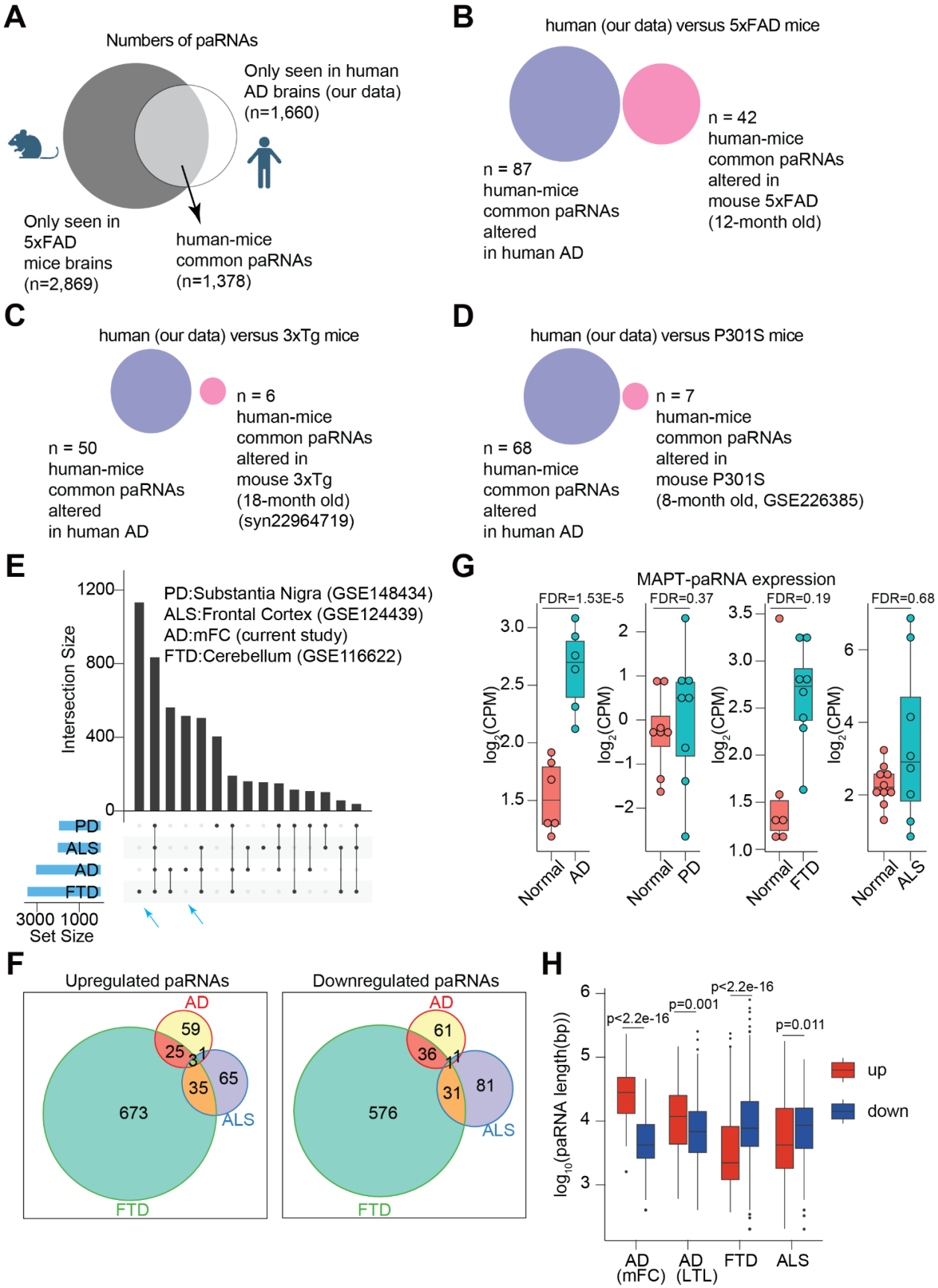
A
Numbers of paRNAs
Only seen in human AD brains (our data) (n=1,660)
Only seen in 5xFAD mice brains (n=2,869)
human-mice common paRNAs (n=1,378)
B
human (our data) versus 5xFAD mice
n = 87 human-mice common paRNAs altered in human AD
n = 42 human-mice common paRNAs altered in mouse 5xFAD (12-month old)
C
human (our data) versus 3xTg mice
n = 50 human-mice common paRNAs altered in human AD
n = 6 human-mice common paRNAs altered in mouse 3xTg (18-month old) (syn22964719)
D
human (our data) versus P301S mice
n = 68 human-mice common paRNAs altered in human AD
n = 7 human-mice common paRNAs altered in mouse P301S (8-month old, GSE226385)
E
PD:Substantia Nigra (GSE148434)
ALS:Frontal Cortex (GSE124439)
AD:mFC (current study)
FTD:Cerebellum (GSE116622)
Intersection Size
Set Size
PD
ALS
AD
FTD
G
MAPT-paRNA expression
FDR=1.53E-5
FDR=0.37
FDR=0.19
FDR=0.68
log2(CPM)
Normal
AD
PD
FTD
ALS
F
Upregulated paRNAs
Downregulated paRNAs
AD
ALS
FTD
59
25
31
35
65
673
61
36
11
31
81
576
H
p<2.2e-16
p=0.001
p<2.2e-16
p=0.011
log10(paRNA length(bp))
up
down
AD (mFC)
AD (LTL)
FTD
ALS

294

295 **Figure 3. Comparing paRNA changes in human AD versus mouse AD models or other human**
296 **neurodegenerative diseases.** **A**. A venn diagram showing the numbers of human-mice common and species-
297 specific paRNAs in human and mouse brains, respectively. The human data is from our current work. The mouse
298 data is calculated from RNA-seq datasets generated in brains of a 5xFAD mouse model. Common paRNAs were
299 defined by their production from promoters of homologous genes. **B-D**. Venn diagrams showing dysregulated
300 paRNAs from human-mouse common paRNAs in either human brains or mouse models as indicated. **E**. An UpSet
301 plot showing common and unique paRNAs detected in human brain RNA-seq data generated in donors bearing
302 several neurodegenerative diseases. The datasets information and brain regions are indicated. Blue arrows point to
303 paRNAs uniquely seen in FTD and AD. **F**. Venn diagrams showing the limited overlaps of upregulated and
304 downregulated paRNAs across different neurodegenerative diseases, respectively. **G**. Boxplots showing the
305 expression levels of *MAPT-paRNA* across different neurodegenerative diseases. FDR values were calculated by
306 DESeq2. **H**. Boxplots showing the length of upregulated and downregulated paRNAs across different
307 neurodegenerative diseases. Red and blue boxplots represent upregulated and downregulated paRNAs in each
308 disease, respectively. P values were calculated by a two-tailed non-parametric Wilcoxon–Mann–Whitney test. In all
309 panels, boxplots indicate the interquartile range with the central line representing the median, and the vertical lines
310 extending to the extreme values in the group.
311
312 We next examined whether any paRNAs are also dysregulated in human brains with other
313 neurodegenerative diseases, such as Parkinson's disease (PD)[49], Frontotemporal Dementia (FTD)
314 [50], and Amyotrophic lateral sclerosis (ALS)[51]. For these, we retrieved RNA-seq datasets for each
315 disease, and identified 1,826 paRNAs in PD, 3,454 in FTD, and 2,007 paRNAs in ALS,
316 respectively, by *de novo* transcript calling (**Fig. 3E**). These paRNAs showed non-overlapping
317 expression patterns in different diseases: for example, more than 500 and 1,000 paRNAs are only
318 found in AD and FTD brain samples, respectively (blue arrows, **Fig. 3E**). We identified
319 deregulated paRNAs in each disease, and these showed limited overlaps (**Fig. 3F**). These results
320 demonstrate disease-specific expression or deregulation of paRNAs, although the contribution of
321 RNA sample quality and different brain regions used in the data generation cannot be fully
322 excluded. For example, *MAPT-paRNA* is expressed in several diseases, but it is upregulated only
323 in the human AD brains (**Fig. 3G**, also see **Fig. 2E**). We observed that the length of upregulated
324 paRNAs was longer than that of downregulated paRNAs in AD brains, which is reproducible by
325 analyzing data from Nativio et al.[36] (**Fig. 3H**). Interestingly, this pattern was not seen or even
326 reversed in ALS and FTD (**Fig. 3H**). These results indicate that paRNAs can be deregulated in
327 several neurodegenerative diseases, but the exact paRNAs and the mechanisms underlying their
328 deregulation can be disease- or context-dependent.
329
330 **Deregulation of paRNAs in AD does not correlate with promoter epigenetic state changes**
331 As paRNAs and their nearby genes share promoters, their expression levels are expected to be
332 correlated if they are regulated at the transcriptional level by the promoters' epigenetic states
333 (**Supplementary Fig. 6A**). However, when we analyzed AD-associated expression changes of

334 paRNAs versus the bidirectional mRNAs from the same promoters, we observed a poor
335 correlation between upregulated paRNAs versus their bidirectional mRNAs (median correlation
336 coefficient R=-0.01, n = 88 pairs); whereas the correlation between AD-downregulated paRNAs
337 and their bidirectional mRNAs is better but remains modest (median correlation coefficient
338 R=0.42, n = 99) (**Supplementary Fig. 6B**). Two representative examples are given, showing an
339 AD-upregulated paRNA from the *CTCF* gene promoter, and an AD-downregulated paRNA
340 antisense to the *VMA21* gene promoter (**Supplementary Fig. 6C**). This phenomenon was
341 recapitulated in another independent AD dataset from the LTL region[36] (**Supplementary Fig.
342 6D**). Taking *MAPT-paRNA* as an example, while it is consistently upregulated in AD, its
343 neighboring gene *MAPT* was not significantly changed from either of two brain regions/cohorts
344 we analyzed (**Supplementary Fig. 6E,F**). These findings suggest that AD-deregulated paRNAs,
345 especially those upregulated in AD, are likely altered in a manner decoupled from the nearest
346 mRNA genes; and if these paRNAs may have functions, it is unlikely they impact their
347 promoter-sharing nearby genes.
348
349 We further examined the epigenetic states of deregulated paRNAs. Because we found consistent
350 changes of paRNAs in the LTL regions of AD brains from the study by Nativio et al.[36] (**Fig. 2F**),
351 which generated ChIP-seq data for acetylation of histone H3 at residue K27 (H3K27ac), a
352 histone marker for active promoters/enhancers, we thus tested this question in LTL. We found
353 that the H3K27ac signal around TSSs of deregulated paRNAs was not different between Normal
354 and AD brains (**Supplementary Fig. 6G**). This observation was recapitulated by analyzing
355 ChIP-Seq datasets of H3K27ac and tri-methylation of histone H3 lysine 4 (H3K4me3) generated
356 by a separate AD brain cohort (DLPFC regions, Rush Alzheimer's Study) (**Supplementary Fig.
357 6H**). Taking *MAPT* and *TMEM41A* loci as examples, the H3K27ac and H3K4me3 signals on
358 their promoters were similar between Normal and AD brains, despite these two paRNAs being
359 upregulated (**Supplementary Fig. 6I**). In summary, our results indicate that the epigenetic state,
360 at least by the histone markers we examined here at the TSSs, is not associated with paRNA
361 deregulation in AD.
362
363 **Cell-type specific paRNA expression and deregulation in AD**

364 Brain tissue consists of several neuronal and glial cell types. We reanalyzed a publicly available
365 single-nucleus RNA-seq (snRNA-seq) dataset generated from Normal/AD human brains[52]
366 (DLPFC region) to appreciate expression patterns of paRNAs in different cell types. Different
367 numbers of Unique Molecular Identifiers (UMIs) and cells of each major type were observed
368 (**Supplementary Fig. 7A,B**). In total, 763 and 872 paRNAs we identified by bulk RNA-seq data
369 of mFC can be detected by DLPFC snRNA-seq in Normal or AD conditions, respectively
370 (**Supplementary Fig. 7C**), among which, m6A-marked paRNAs were more detectable
371 (**Supplementary Fig. 7D,E**). These numbers were broken down to cell-type-specific patterns,
372 and excitatory neurons (Ex) possess the largest numbers of paRNAs detected (**Supplementary**
373 **Fig. 7F**). Among paRNAs seen in snRNA-seq data, about 30% (n=284) are exclusively detected
374 in neurons (excitatory, Ex; or inhibitory, In), and a smaller group of paRNAs (n=69) are
375 exclusively detected in glial cell types (such as astrocytes, Ast; oligodendrocytes, Oli; or
376 microglia, Mic; **Supplementary Fig. 7F**). For the top five highly AD-upregulated paRNAs (**Fig.**
377 **2E**), they all displayed a certain degree of cell-type-specificity (**Supplementary Fig. 7G**). For
378 example, *DOCK7-paRNA* was highly expressed in Ast; *MAPT-paRNA* is expressed higher in Ex
379 and In, and to some degree in Oli (**Supplementary Fig. 7G**). By comparing Normal and AD
380 conditions in each cell type, *MAPT-paRNA* was significantly increased in AD only in Ex
381 (**Supplementary Fig. 7H**). This paRNA is annotated as *MAPT-AS1* in the Gencode database, but
382 for consistency in this paper, we will refer to it as *MAPT-paRNA*. These results indicate that
383 paRNAs are expressed in the human brain and altered in AD with cell-type-specificity.
384

385 **m6A methylation regulates stability of paRNAs**

386 We searched for appropriate cell models to study the potential roles of AD-associated paRNAs
387 and the impact of m6A. In major iPSC-derived brain cells where RNA-seq data are available[53],
388 each of the top five AD-deregulated paRNAs was found to display some level of cell-type-
389 specificity, but they are more often expressed highly in neurons (**Supplementary Fig. 8A**).
390 Among these, *MAPT-paRNA* exhibited the highest and almost exclusive expression in iPSC-
391 derived neurons (**Supplementary Fig. 8A**). It is notable that the cell-type-specificity of paRNAs
392 revealed by DPFLC snRNA-seq data differs from that by bulk RNA-seq from iPSC derived cells
393 (**Supplementary Figs. 7G, 8A**), indicating that cell models can only partially recapitulate
394 paRNA expression patterns in adult and/or AD human brains.

395 *MAPT* is a central disease locus in AD, because it encodes for the Tau protein that drives
396 neurofibrillary tangles in AD brains[3]. A previous study reported that *MAPT* nature antisense
397 transcript (NAT), which largely overlaps and is essentially *MAPT-paRNA*, represses *MAPT*
398 translation to Tau protein in SH-SY5Y cell line[33]. However, another study found that *MAPT-*
399 *paRNA* does not impact *MAPT*/Tau at either the transcriptional or translational levels[34].
400 Consequently, the functional role of *MAPT-paRNA* in AD remains unclear. We thus elected to
401 focus on *MAPT-paRNA* for in depth experimental studies. We first tested the expression of
402 *MAPT-paRNA* in cellular models, including human embryonic stem cells (H1-ESCs), a human
403 microglia cell line (HMC3), a human neuroblastoma cell line (SH-SY5Y), H1-hESC-derived
404 astrocytes, neural progenitor cells (NPC), and iPSC-derived microglia and neurons (i3Neurons)
405 (see methods, **Fig. 4A**). Quantitative reverse-transcription PCR (qRT-PCR) results confirmed
406 that *MAPT-paRNA* is highly and almost exclusively expressed in i3Neurons as compared to other
407 cell types (**Fig. 4A**). The i3Neurons we generated are based on a doxycycline (Dox) inducible
408 NGN2-directed differentiation method of WTC11 iPSCs[54], which are glutamatergic excitatory
409 neurons that displayed well-recognized neuronal maturation processes by both morphology and
410 molecular markers (**Supplementary Fig. 8B,C**). Three weeks after in vitro differentiation (IVD),
411 these neurons started to express *MAP2*, a neuronal marker, and by 6-8 weeks, they showed
412 prominent expression of synaptic markers, such as postsynaptic density protein 95 (PSD95)
413 (**Supplementary Fig. 8B,C**). *MAPT-paRNA* appeared to gradually increase expression during
414 neuronal maturation and its level plateaued at around 5 weeks IVD (**Supplementary Fig. 8D**).
415 To investigate how m6A methylation may impact *MAPT-paRNA* expression, we treated 8-week-
416 old i3Neurons with STM2457[55], a chemical inhibitor of m6A writer METTL3. Antibody based
417 m6A RIP-qPCR showed that this treatment reduced the m6A methylation level of *MAPT-*
418 *paRNA*, which resulted in its expression decrease as shown by RT-qPCR (**Fig. 4B,C**). These
419 results suggest that m6A positively regulates *MAPT-paRNA* expression. In contrast, this
420 treatment did not impact either the mRNA expression or transcription level of *MAPT*, which
421 shares the same promoter with the paRNA. These are revealed by using primers targeting the
422 mRNA (across exons) or the intronic regions (indicating pre-mRNA transcription), respectively
423 (**Supplementary Fig. 8E**). These results indicate that m6A inhibition did not reduce *MAPT-*
424 *paRNA* level via altering the transcriptional activity of the shared promoter, which otherwise
425 would have affected *MAPT* transcription as well. We further examined if the observed *MAPT-*

426 *paRNA* reduction takes place at the RNA stability level, and found that after transcriptional
427 inhibition, the paRNA with a lower m6A level (i.e., presence of STM2457) displayed a lower
428 stability and faster decay (**Fig. 4D**). We additionally conducted genetic knockdown (KD) of
429 METTL3 by an antisense oligonucleotide (ASO) in 8-week old i3Neurons (**Supplementary Fig.**
430 **8F,G**), which reduced both m6A modification and RNA expression level of *MAPT-paRNA*
431 (**Supplementary Fig. 8H,I**), consistent with the results from the chemical inhibitor treatment.
432
433 ***MAPT-paRNA* regulates global gene transcription in human neurons *in cis* and *in trans***
434 We further studied the functions of *MAPT-paRNA* by employing ASOs to KD it in 8-week IVD
435 excitatory i3Neurons, because at this stage, neurons possess maximal level of expression of this
436 paRNA, displaying prominent neuronal morphology and synaptic features (**Supplementary Fig.**
437 **8B,C**). Gymnotic delivery of ASO achieved potent KD of *MAPT-paRNA* (>80% reduction)
438 without affecting neuronal viability or morphology (**Fig. 4E, and Supplementary Fig. 9A**). We
439 found that KD of *MAPT-paRNA* did not alter *MAPT*/Tau at either the transcriptional or
440 translational levels in i3Neurons (no matter if it is the mRNA, the Tau protein, or the
441 phosphorylated Tau (p-Tau) that is implicated in AD pathology), even after an extended 7-day
442 KD (**Supplementary Fig. 9B,C**). This indicates that *MAPT-paRNA* did not regulate the
443 neighboring gene, *MAPT*, consistent with the report by Policarpo, et al.[34]. No change of
444 *MAPT*/Tau was seen after the KD of *MAPT-paRNA* in SH-SY5Y cells, either (a neuroblastoma
445 cell model used by a prior study of MAPT-paRNA[33]) (**Supplementary Fig. 9D,E**). This result is
446 consistent with the fact that paRNAs upregulated in AD show poor correlation with changes of
447 their bidirectional mRNAs (**Supplementary Fig. 6A,B,D,E,F**).

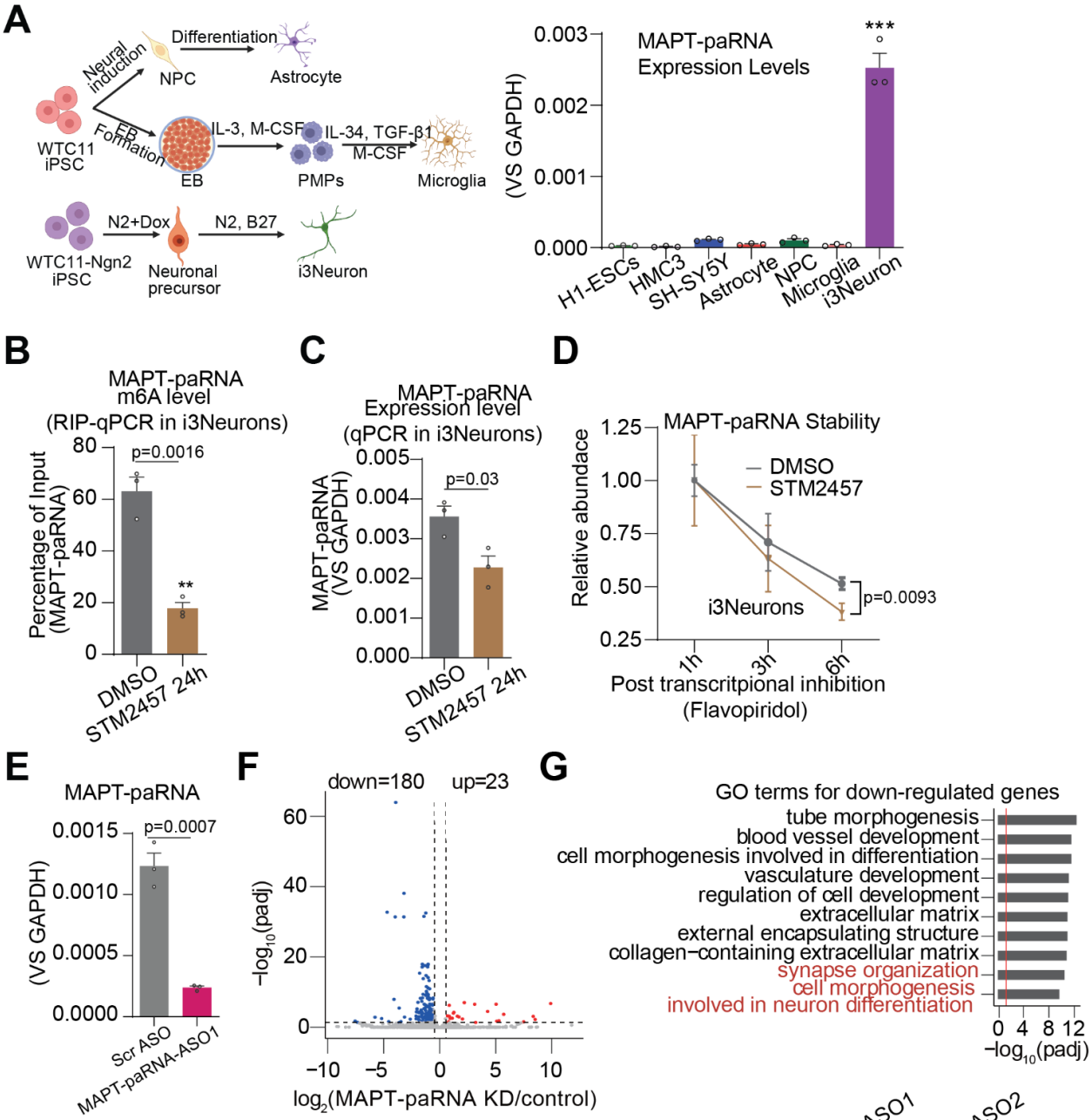
A
Neural induction
Differentiation
NPC
Astrocyte
WTC11 iPSC
EB Formation
IL-3, M-CSF
IL-34, TGF-β1
M-CSF
EB
PMPs
Microglia
WTC11-Ngn2 iPSC
N2+Dox
N2, B27
Neuronal precursor
i3Neuron
MAPT-paRNA Expression Levels
(VS GAPDH)
0.003
0.002
0.001
0.000
***
H1-ESCs
HMC3
SH-SY5Y
Astrocyte
NPC
Microglia
i3Neuron
B
MAPT-paRNA m6A level (RIP-qPCR in i3Neurons)
Percentage of Input (MAPT-paRNA)
p=0.0016
**
DMSO
STM2457 24h
C
MAPT-paRNA Expression level (qPCR in i3Neurons)
MAPT-paRNA (VS GAPDH)
p=0.03
DMSO
STM2457 24h
D
MAPT-paRNA Stability
Relative abundace
DMSO
STM2457
i3Neurons
p=0.0093
1h
3h
6h
Post transcritpional inhibition (Flavopiridol)
E
MAPT-paRNA
(VS GAPDH)
p=0.0007
Scr ASO
MAPT-paRNA-ASO1
F
down=180
up=23
−log10(padj)
log2(MAPT-paRNA KD/control)
G
GO terms for down-regulated genes
tube morphogenesis
blood vessel development
cell morphogenesis involved in differentiation
vasculature development
regulation of cell development
extracellular matrix
external encapsulating structure
collagen−containing extracellular matrix
synapse organization
cell morphogenesis
involved in neuron differentiation
−log10(padj)
H
SYNGAP1
MEF2C
HDAC4
(VS GAPDH)
p=0.027
p<0.0001
p=0.0004
Scr ASO
MAPT-paRNA-ASO1
I
Scr ASO
MAPT-paRNA-ASO1
MAPT-paRNA-ASO2
1 2 3 4 5 6 7 8 9
SYNGAP1
MEF2C
HDAC4
GAPDH

448

449 **Figure 4. Neuron-enriched *MAPT-paRNA* stability control by m6A and its global regulatory functions. A.**
450 (Left) Cartoon diagrams illustrating the differentiation of iPSC-derived brain cells (created with BioRender.com).
451 (Right) A barplot showing the expression levels of *MAPT-paRNA* in various cell types. P value was calculated by a
452 two-tailed student's t-test. **B,C**. MeRIP-qPCR and RT-qPCR data showing m6A methylation and *MAPT-paRNA*
453 expression with and without STM2457 treatment, respectively. **D**. Time course stability of *MAPT-paRNA* measured
454 by RT-qPCR after transcriptional inhibition, with and without STM2457 pre-treatment for 24hr. P value was
455 calculated by a two-tailed student's t-test. **E**. A barplot showing the relative RNA expression of *MAPT-paRNA*
456 quantified by RT–qPCR after scramble or targeting ASO treatment. **F**. A volcano plot showing differentially
457 expressed genes after *MAPT-paRNA* knockdown using a targeting ASO versus the scramble ASO treatment. Red
458 and blue dots represent upregulated and downregulated genes, respectively. **G**. GO analysis for the downregulated
459 genes after *MAPT-paRNA* knockdown. The red line represents adjusted p values (padj) at 0.05. **H**. Barplots showing
460 relative RNA expression of *MEF2C*, *SYNGAP1*, and *HDAC4* quantified by RT–qPCR. P values were calculated by a
461 two-tailed student's t-test. **I**. Protein levels of *MEF2C*, *SYNGAP1*, and *HDAC4* showing triplicates of Western
462 blotting (WB) after *MAPT-paRNA* knockdown.
463

464 To unbiasedly explore its functions, we performed RNA-seq after *MAPT-paRNA* KD. This
465 revealed over 200 genes deregulated, with most of them showing downregulation (n=180), and a
466 smaller subset upregulation (n=23) (**Fig. 4F,** and **Supplementary Table 8**). RNA-seq also
467 confirmed qPCR data that *MAPT* mRNA was not changed (**Supplementary Figs.9B,10A**). GO
468 analysis revealed that the functions of these downregulated genes are closely related to synaptic
469 functions (**Fig. 4G**, and **Supplementary Table 9**). Among these, some are known to be
470 important regulators of neuronal/synaptic biology, such as *SYNGAP1*[56], *MEF2C*[57], and *HDAC4*[58]
471 (**Supplementary Fig. 10B,C,D**). We validated the expression reduction of these "target genes"
472 of *MAPT-paRNA* by RT-qPCR (**Fig. 4H**) and by a second ASO (**Supplementary Fig. 10E**).
473 Consistently, the protein levels encoded by these target genes were also decreased (**Fig. 4I**, and
474 **Supplementary Fig. 10F**). These results demonstrated that *MAPT-paRNA* is a global regulator
475 of gene expression that selectively impacts neuronal/synaptic functions. Interestingly, very few
476 of these target genes are located in its genomic vicinity, and most of them are on different
477 chromosomes (**Supplementary Fig. 10G**), suggesting that *MAPT-paRNA* regulates target gene
478 expression both *in cis* and *in trans*. This is a distinct function from the reported action of some
479 paRNAs that impacts the bidirectional gene sharing promoter with them[27,28].
480

481 **Functional paRNA-target-gene interactions in 3D nucleus revealed by single-cell RNA-**
482 **DNA interactome**

483 A plausible mechanism underlying paRNAs' roles in gene expression control is that they may
484 directly interact with target genes via spatial proximity in a 3D nucleus. To explore this, we
485 analyzed recent single nuclei RNA-DNA interactome data of the human brain (DLPFC region),

486 namely by the Multi-Nucleic Acid Interaction Mapping in Single Cell (MUSIC) technique[59]
487 (**Fig. 5A**). MUSIC employs cell barcodes (CB) to define molecules (DNA or RNA) from the
488 same cell, and then uses molecular barcodes (MB) to identify shared molecular complexes that
489 define interactions of DNAs or RNAs (**Fig. 5A**, **see methods**). It provides single cell RNA-DNA
490 interactome and thus can reveal paRNAs' cell-type specific target genes. The cell numbers and
491 gene expression counts from our analysis of the MUSIC datasets are shown in **Supplementary**
492 **Fig. 11A,B** and are identical to what was originally reported[59].
493
494 Overall, 425 paRNAs can be detected in MUSIC data in at least one of the cell types. Among
495 these, Ex exhibited the largest number of detectable paRNAs (n = 393, **Fig. 5B**). This is perhaps
496 partially because our paRNA list was identified in bulk brain RNA-seq data in which neuronal
497 signals are dominant [38], and partially it may also be due to higher detectable RNA reads in Ex in
498 MUSIC data (**Supplementary Fig. 11A,B**). For each paRNA, MUSIC identified their interacting
499 genes in the 3D nucleome based on shared CBs and MBs (**Fig. 5A, see methods**). Ex and Ast
500 exhibited 106 and 17 paRNAs that are specific/exclusive to these two cell types, respectively
501 (**Fig. 5B**). We identified genes showing RNA-DNA contacts with these cell-type-specific
502 paRNAs in their respective cell types, and found 4,736 interacting genes for Ex-specific paRNAs
503 and 1,055 genes for Ast-specific paRNAs. GO analysis of these paRNA-interacting genes
504 revealed them to be related to neuron differentiation/synapse in Ex and cell-cell adhesion in Ast
505 (**Supplementary Fig. 11C**), respectively, suggesting that cell-type-specific paRNAs may play
506 roles in regulating cell-type-specific genes and cellular functions.

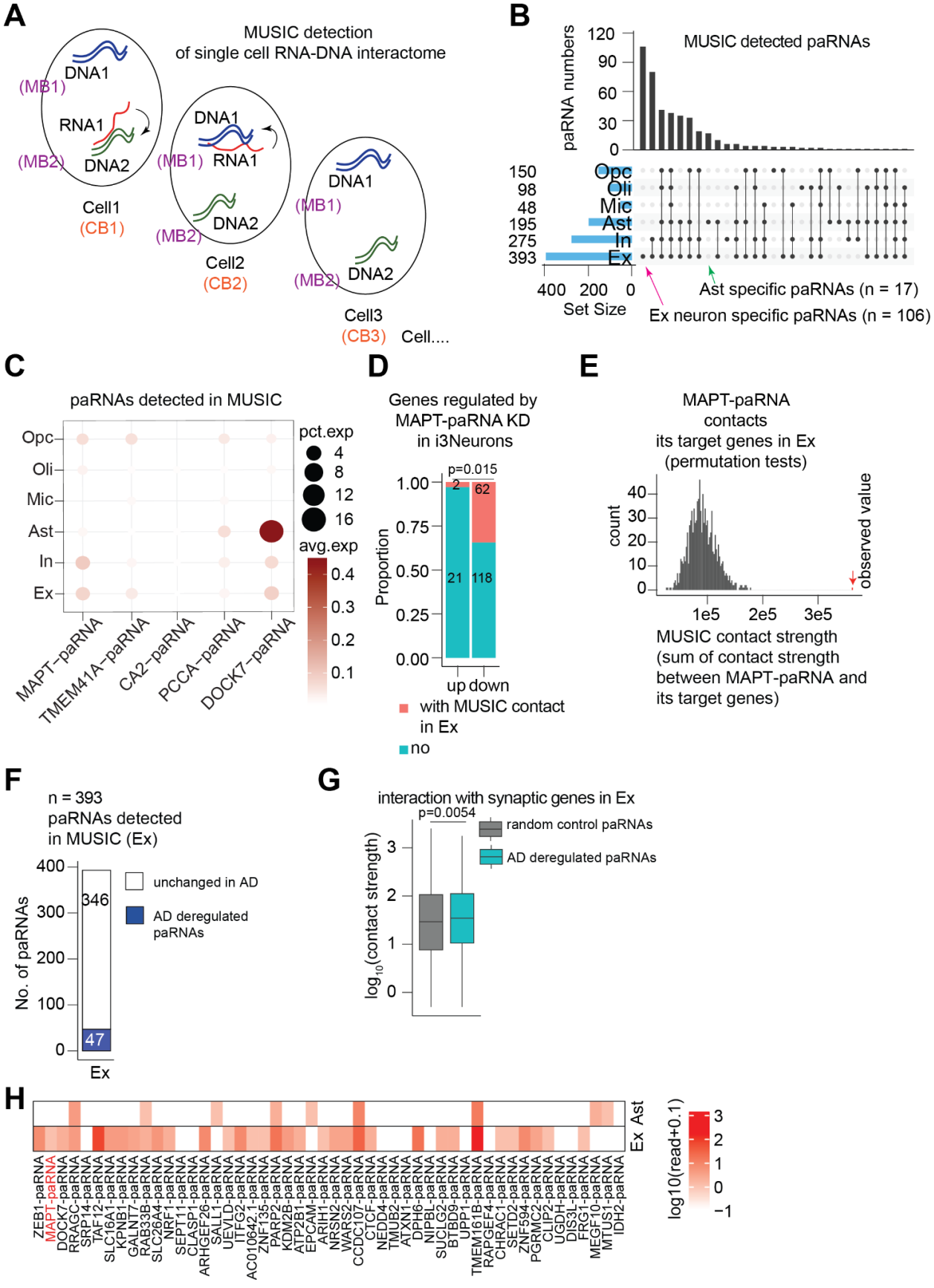
A
MUSIC detection
of single cell RNA-DNA interactome
DNA1
(MB1)
RNA1
(MB2)
DNA2
Cell1
(CB1)
DNA1
(MB1)
RNA1
DNA2
(MB2)
Cell2
(CB2)
DNA1
(MB1)
DNA2
(MB2)
Cell3
(CB3)
Cell....
B
MUSIC detected paRNAs
paRNA numbers
120
90
60
30
0
150
98
48
195
275
393
Opc
Oli
Mic
Ast
In
Ex
400
200
0
Set Size
Ast specific paRNAs (n = 17)
Ex neuron specific paRNAs (n = 106)
C
paRNAs detected in MUSIC
Opc
Oli
Mic
Ast
In
Ex
MAPT−paRNA
TMEM41A−paRNA
CA2−paRNA
PCCA−paRNA
DOCK7−paRNA
pct.exp
4
8
12
16
avg.exp
0.4
0.3
0.2
0.1
D
Genes regulated by
MAPT-paRNA KD
in i3Neurons
p=0.015
2
62
21
118
1.00
0.75
0.50
0.25
0.00
Proportion
up
down
with MUSIC contact
in Ex
no
E
MAPT-paRNA
contacts
its target genes in Ex
(permutation tests)
count
40
30
20
10
0
observed value
1e5
2e5
3e5
MUSIC contact strength
(sum of contact strength
between MAPT-paRNA and
its target genes)
F
n = 393
paRNAs detected
in MUSIC (Ex)
400
300
200
100
0
No. of paRNAs
346
47
Ex
unchanged in AD
AD deregulated
paRNAs
G
interaction with synaptic genes in Ex
p=0.0054
random control paRNAs
AD deregulated paRNAs
3
2
1
0
log10(contact strength)
H
Ex
Ast
ZEB1-paRNA
MAPT-paRNA
DOCK7-paRNA
RRAGC-paRNA
SRP14-paRNA
TAF12-paRNA
SLC16A1-paRNA
KPNB1-paRNA
GALNT7-paRNA
RAB33B-paRNA
SLC26A4-paRNA
NRF1-paRNA
SEPT11-paRNA
CLASP1-paRNA
ARHGEF26-paRNA
SALL1-paRNA
UEVLD-paRNA
ITFG2-paRNA
AC010642.1-paRNA
ZNF135-paRNA
PARP2-paRNA
KDM2B-paRNA
ATP2B1-paRNA
EPCAM-paRNA
ARIH1-paRNA
NRSN2-paRNA
WARS2-paRNA
CCDC107-paRNA
CTCF-paRNA
NEDD4-paRNA
TMUB2-paRNA
ATXN1-paRNA
DPH6-paRNA
NIPBL-paRNA
SUCLG2-paRNA
BTBD9-paRNA
UPP1-paRNA
TMEM161B-paRNA
RAPGEF4-paRNA
CHRAC1-paRNA
SETD2-paRNA
ZNF594-paRNA
PGRMC2-paRNA
CLIP2-paRNA
UGDH-paRNA
DIS3L-paRNA
FRG1-paRNA
MEGF10-paRNA
MTUS1-paRNA
IDH2-paRNA
log10(read+0.1)
3
2
1
0
−1

507

508 **Figure 5. paRNA-DNA interaction in human brain cells revealed by MUSIC data. A**. A diagram showing
509 RNA-DNA interaction at single-cell level in MUSIC data using cell barcodes (CB) and molecular barcodes (MB).
510 CB is shared by all molecules in one cell, and MB is shared by all molecules in one molecular complex. **B.** An
511 UpSet plot showing paRNAs and their numbers (to the left) in different cell types detected by MUSIC from Normal
512 brain. **C**. A dotplot showing the average expression of the top five AD-upregulated paRNAs in MUSIC data. Ex:
513 Excitatory neurons. In: Inhibitory neurons. Ast: Astrocyte. Mic: Microglia. Oli: Oligodendrocyte. Opc:
514 Oligodendrocyte progenitor cell. **D**. A barplot showing the numbers of differentially expressed genes seen after
515 MAPT-paRNA KD that form RNA-DNA interactions with *MAPT-paRNA* in the Ex neurons. P value: Fisher's exact
516 test. **E**. A barplot from permutation test showing the observed contact strength between MAPT-paRNA and its true
517 62 target genes (red arrow to the right) versus contact strength between MAPT-paRNA and 1000 sets of randomly
518 selected 62 genes. **F**. A barplot showing the number of paRNAs detected by MUSIC data in Ex neurons and the
519 subset that show AD-deregulation in bulk RNA-seq data in Fig.2. **G**. A boxplot showing the RNA-DNA contact
520 strength between the two groups of paRNAs and synaptic genes in Ex: AD-deregulated paRNAs (n = 47 in panel F),
521 and non-AD-deregulated paRNAs (n = 346). P value: two-tailed non-parametric Wilcoxon–Mann–Whitney test.
522 Boxplots indicate the interquartile range with the central line representing the median, and the vertical lines
523 extending to the extreme values in the group. **H**. A heatmap showing the RNA-DNA contact strength between AD-
524 deregulated paRNAs and a single *MEF2C* gene detected in Ex and Ast, respectively.
525
526 We found that m6A-paRNAs can be better detected by the MUSIC data than non-m6A-modified
527 paRNAs, and this is consistent in all cell types (**Supplementary Fig. 11D,E**). This pattern is
528 similar to that in snRNA-seq data (**Supplementary Fig. 7D,E**). As compared to non-m6A-
529 paRNAs, m6A-paRNAs on average can interact with more genes, and show higher interaction
530 strength with genes they contact, a trend particularly obvious in Ex (**Supplementary Fig. 11F**).
531 These results support a notion that m6A-paRNAs are more detectable in MUSIC data possibly
532 due to higher stability, and they possess higher propensity to act in target gene regulation,
533 particularly in Ex. The top five AD-upregulated paRNAs display expression in two or three cell
534 types in MUSIC data (**Fig. 5C**), again a pattern similar to that revealed by snRNA-seq
535 (**Supplementary Fig. 7G**). As aforementioned, KD of *MAPT-paRNA* in i3Neurons, a model of
536 human excitatory neurons, deregulated ~200 genes (**Fig. 4F,G**), many of which are important for
537 neuron differentiation and synapse organization. To test the mechanisms, we examined if *MAPT-*
538 *paRNA* forms direct RNA-DNA contacts with these "target genes", and we found that about 30%
539 of them (up=2 and down=62) indeed displayed MUSIC RNA-DNA contacts in Ex (**Fig. 5D**).
540 Given that only 2 upregulated genes interact with *MAPT-paRNA*, we will focus on the 62
541 downregulated "target genes" interacting with *MAPT-paRNA*. The observed contact strength
542 between *MAPT-paRNA* and these 62 target genes was much higher than by random chance (**Fig.**
543 **5E**), as shown by permutation tests, for which we randomly selected 62 genes 1,000 times, and
544 calculated the contact strength between *MAPT-paRNA* and each of these random genesets. The
545 contacts between *MAPT-paRNA* and the 62 target genes were more pronounced in Ex than in In

546 or Ast (**Supplementary Fig. 11G**), lending support to the notion that *MAPT-paRNA* contacts
547 these genes and functionally activates their expression specifically in Ex.
548
549 We attempted to test whether this notion may apply to other paRNAs in Ex; i.e., do many of
550 them contact synapse/neuronal genes to potentially play roles in gene regulation and in AD? Out
551 of 393 detectable paRNAs in Ex in MUSIC data, 47 were deregulated in our bulk RNA-seq data
552 (**Fig. 5F**). We calculated RNA-DNA contact strength of each of these paRNAs with a curated set
553 of synapse-associated genes (n = 393, see methods about this curated list), and we found that
554 paRNAs deregulated in AD, as compared to average paRNAs, display higher interaction
555 frequency with synapse-associated genes in Ex (**Fig. 5G**). As an example, RNA-DNA contacts
556 were found in Ex to form between not only *MAPT-paRNA,* but also a series of other AD-
557 deregulated paRNAs, with *MEF2C* (encoding a key neuronal factor known to confer resilience to
558 AD[47,60])(**Fig. 5H**). In contrast, these interactions did not take place in Ast (**Fig. 5H**). These
559 results support that at least a subset of neuronal paRNAs, as exemplified by *MAPT-paRNA*, can
560 contact and regulate neuronal/synapse genes; alteration of such paRNAs in AD are involved in
561 deregulation of key synaptic genes and AD pathogenesis.
562
563 ***MAPT-paRNA* protects neurons from excitotoxicity by modulating synaptic activity**
564 An important feature of AD is neuronal hyperexcitability, which leads to excitotoxicity and
565 neuronal death[61,62]. This is often mediated by an overactive N-methyl-d-aspartate receptor
566 (NMDAR) at the synapse. Several key synaptic genes dependent on *MAPT-paRNA*, such as
567 *MEF2C* and *SYNGAP1* (**Fig. 4G,H**), have been known to modulate NMDA activity at synapses
568 [63-65]. Indeed, *Mef2c* deletion in mice impairs learning and memory[66], and it has been shown to
569 prevent neuronal apoptosis elicited by excitotoxic NMDA[65]. Loss of *SYNGAP1* induces neuronal
570 hyperexcitability, leading to deficits in learning and memory[67]. These results suggest that *MAPT-*
571 *paRNA* might act as a neuroprotective modulator in the context of AD.

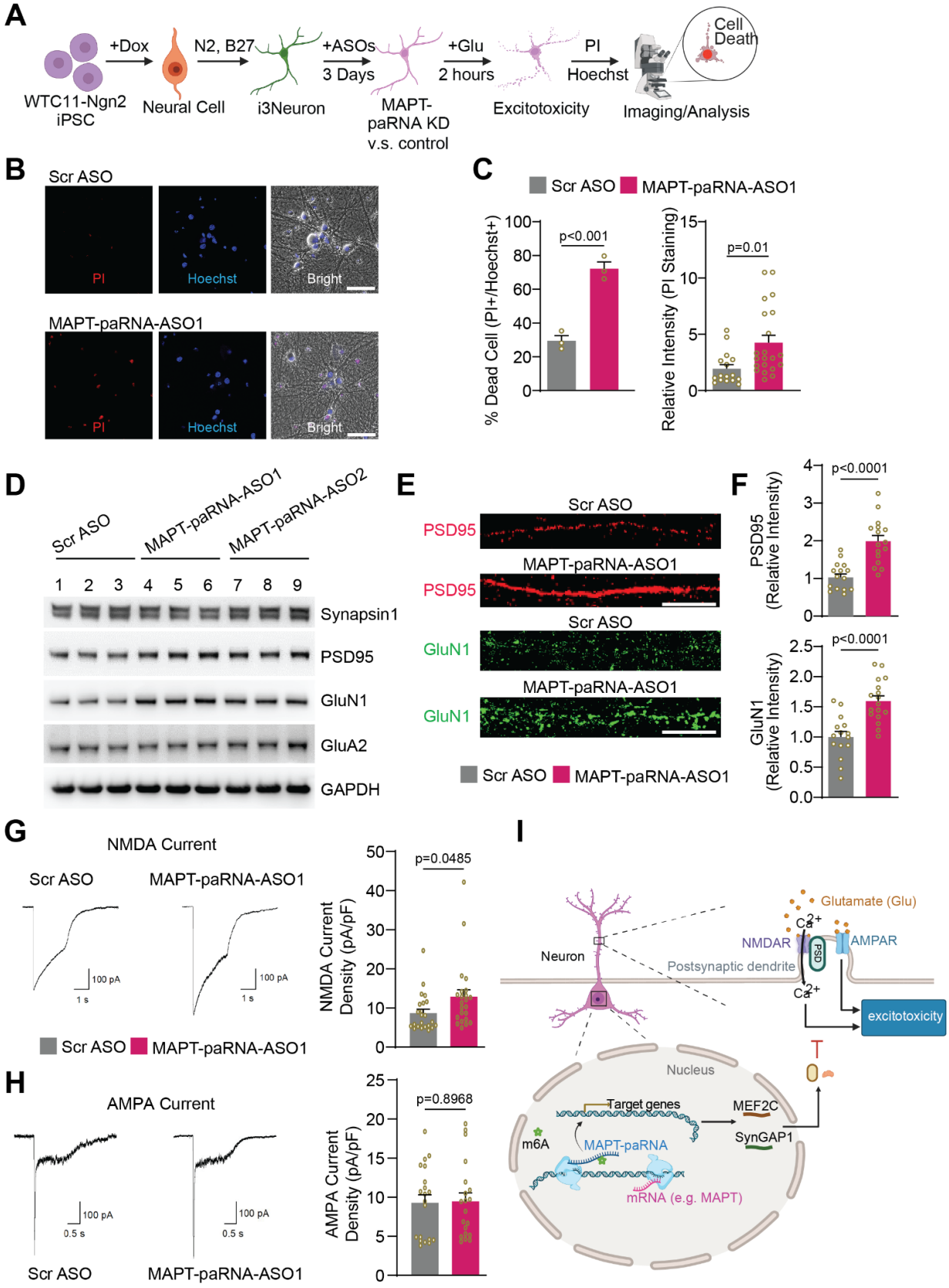
A
+Dox
N2, B27
+ASOs
3 Days
+Glu
2 hours
PI
Hoechst
Cell Death
WTC11-Ngn2 iPSC
Neural Cell
i3Neuron
MAPT-paRNA KD v.s. control
Excitotoxicity
Imaging/Analysis
B
Scr ASO
PI
Hoechst
Bright
MAPT-paRNA-ASO1
C
Scr ASO
MAPT-paRNA-ASO1
% Dead Cell (PI+/Hoechst+)
p<0.001
Relative Intensity (PI Staining)
p=0.01
D
Scr ASO
MAPT-paRNA-ASO1
MAPT-paRNA-ASO2
1 2 3 4 5 6 7 8 9
Synapsin1
PSD95
GluN1
GluA2
GAPDH
E
Scr ASO
PSD95
MAPT-paRNA-ASO1
GluN1
F
PSD95 (Relative Intensity)
p<0.0001
GluN1 (Relative Intensity)
G
NMDA Current
Scr ASO
MAPT-paRNA-ASO1
100 pA
1 s
NMDA Current Density (pA/pF)
p=0.0485
H
AMPA Current
0.5 s
AMPA Current Density (pA/pF)
p=0.8968
I
Neuron
Glutamate (Glu)
NMDAR
AMPAR
PSD
Postsynaptic dendrite
excitotoxicity
Nucleus
Target genes
MEF2C
SynGAP1
m6A
MAPT-paRNA
mRNA (e.g. MAPT)

572

573 **Figure 6. The neuroprotective role of *MATP-paRNA* against excitotoxicity. A**. Schematic representation of
574 glutamate toxicity in WTC11-derived i3Neurons. 8-week-old i3Neurons with/without *MAPT-paRNA* knockdown
575 were treated with 10μM glutamate for 2 hours. PI (propidium iodide) and Hoechst 33342 were introduced to the
576 medium to visualize dead (PI+) and total (Hochest+) cells, respectively. **B.** Representative images showing
577 glutamate-induced i3Neuron cell death after *MAPT-paRNA* knockdown. Scale bar, 50μm. **C**. Quantification of
578 apoptotic i3Neurons from panel B. **D**. Triplicates of western blot analysis of synaptic markers (Synapsin1 and
579 PSD95) and glutamate receptors (GLUN1 and GLUA2) in i3Neurons after *MAPT-paRNA* knockdown. **E**.
580 Representative images showing immunofluorescent signals of PSD95 and GluN1 at the dendrites of i3Neurons after
581 *MAPT-paRNA* knockdown, showing their accumulation. Scale bar, 10μm. **F.** Quantitative analysis of signals in
582 panel **E**. For each group, at least 15 neurons from 3 different experiments were quantified and analyzed. **G.**
583 Representative NMDA current traces (left panel) and current density comparison (right panel) from i3Neurons
584 treated with scramble control and *MAPT-paRNA* ASO1 (n = 23 neurons per group). **H**. Representative AMPA
585 current traces (left panel) and current density comparison (right panel) from i3Neurons treated with scramble control
586 and *MAPT-paRNA* ASO1 (n = 20 neurons per group). **I**. A model of *MAPT-paRNA* function, as a representative
587 m6A-modified ncRNA in AD, in neuronal gene regulation and survival (generated by Biorender). P values: two-
588 tailed unpaired student's t-tests were used for **C, F**, **G**, and **H**.
589

590 To test this, we employed an AD-relevant glutamate-induced excitotoxicity model[68,69] (**Fig. 6A**).
591 We found that mature i3Neurons (8-week IVD) with *MAPT-paRNA* KD are more vulnerable to
592 glutamate-induced cell apoptosis, as shown by significantly higher numbers of cells showing
593 Propidium Iodide (PI) staining (**Fig. 6B,C**). Since SYNGAP1 and MEF2C have been reported to
594 inhibit excitotoxicity by modulating the levels of postsynaptic proteins and glutamate receptors,
595 we selected four of these proteins/receptors to test, finding PSD95 and GluN1 (glutamate NMDA
596 Receptor 1) significantly increased in i3Neurons after *MAPT-paRNA* knockdown, while
597 Synapsin1 (a presynaptic protein) and GluA2 (glutamate AMPA Receptor subunit 2) were not
598 changed (**Fig. 6D**, and **Supplementary Fig. 12A**). These changes did not take place at the
599 mRNA levels (**Supplementary Fig. 12B,C**), consistent with the reports that SYNGAP1 or
600 MEF2C modulate post-synapse proteins and excitability locally at the synapse[70,71]. We also
601 conducted KD of *MEF2C* and *SYNGAP1* mRNAs by ASOs, and these caused upregulation of
602 PSD95 and GluN1, but not GluA2, a pattern consistent with *MAPT-paRNA* KD (**Supplementary**
603 **Fig. 12D,E,F**). Furthermore, immunostaining after *MAPT-paRNA* KD directly showed
604 accumulation of PSD95 and GluN1 at the dendrites of i3Neurons (**Fig. 6E,F**). Importantly,
605 neuronal electrophysiology confirmed alteration of NMDA receptor activity after KD of this
606 paRNA, while AMPA receptor activity was unaffected (**Fig. 6G,H**). The protective role of
607 *MAPT-paRNA* also applies to beta-amyloid (Aβ-42)-induced neuronal cytotoxicity[72,73], as
608 revealed by increased lactate dehydrogenase (LDH) release in the culture media if i3Neurons
609 were depleted of this paRNA (**Supplementary Fig. 12G**). All together, these results indicate that
610 *MAPT-paRNA* exerts neuroprotective effects, at least in part, via regulating the expression of key

synapse-associated genes to modulate the distribution and assembly of synaptic scaffolding proteins and glutamate receptors (**Fig. 6I**).

Discussion

m6A methylome on coding and noncoding RNAs in human brain and AD

Our current study utilized total RNA-seq and m6A RIP-seq datasets in human brain samples from AD patients or cognitively normal controls, and identified a comprehensive landscape of RNA m6A methylome on mRNAs and ncRNAs. Our results showed that about 60-70% of m6A peaks in the human mFC are located in the noncoding regions (**Fig.1A,** and **Supplementary Fig. 2H**), encompassing various categories of ncRNAs. These include annotated lncRNAs or other ncRNAs (e.g., snoRNAs and snRNAs), as well as ncRNAs that have not been previously annotated in the human transcriptome (Gencode database), including many paRNAs that we focused on in the latter part of this work. Interesting, we observed around 8,000 highly m6A-marked intronic regions that overlap with L1 elements. These intronic m6A-marked L1s have been identified by our previous work in cancer cells, fetal human brains, and iPSC-derived neural progenitor cells[12], in which we dubbed them m6A-marked intronic L1s (MILs) and found they can impact the transcription of the genes that harbor them. While in this current work we focus on paRNAs for functional studies because they have been less explored, it will be interesting and important to further test the roles of various m6A-modified ncRNAs in gene regulation, cellular functions in the human brain, and in AD pathogenesis. Therefore, our current work offers an m6A methylome that has significantly extended the previous observations of m6A on mRNAs in normal human brains or in diseased brains from AD or ALS[19,74].

Our RNA-seq transcriptome data captured known features of the AD brain, including reduced expression of synapse-related genes, and this pattern is consistent with other recent datasets[36]. Interestingly, the changes of m6A methylome in normal and AD conditions are not particularly pervasive, i.e., we identified 835 and 1,645 regions showing m6A hypo- and hyper-methylation. This selective and moderate m6A change in AD is consistent with the fact that we did not observe strongly changed gene expression of m6A modifying enzyme genes in AD brains, such as *METTL3* and *METTL14.* In addition, we observed a moderate but significant positive correlation between m6A changes and ncRNA expression changes (**Supplementary Fig. 4A,B**).

642 This indicates that collectively m6A modification may play a positive role in regulating ncRNA
643 expression in human brains. However, it is noteworthy that m6A is by no means the only
644 mechanism that impacts the expression of these ncRNAs in the brain or in AD, and thus it is not
645 surprising that the positive correlation is not particularly strong. Knockdown of METTL3, the
646 main m6A enzyme, quantitatively affected *MAPT-paRNA* expression (**Supplementary Fig.**
647 **8F,G,I**). Other mechanisms affecting ncRNA expression in AD can be from the levels of
648 transcriptional/epigenetic control and other non-m6A-mediated RNA stability regulation.
649
650 **Expression patterns and regulation of paRNAs in neurodegeneration**
651 We identified 3,038 paRNAs in the human brain mFC region via *de novo* transcript calling, and
652 found that close to 40% of them harbor m6A methylation. Interestingly, the genes neighboring
653 m6A-marked paRNAs show enrichment of terms like synapses, indicating that paRNAs are
654 produced and methylated selectively from important synapse/brain associated loci. By
655 comparing paRNA landscapes we detected in human AD brain with those from mouse AD
656 models, or from brain samples with other neurodegenerative diseases (NDDs), our study
657 supports a conclusion that human AD-associated paRNAs are quite unique to human AD, and
658 not commonly seen changed in other NDDs that we analyzed. These results demonstrate that
659 paRNAs are potentially disease specific ncRNAs that play roles in gene dysregulation or disease
660 etiology of NDDs.
661
662 Our analysis of available epigenetic datasets supports that AD-deregulated paRNAs, particularly
663 those that show upregulation in AD, are unlikely to be altered at the epigenetic levels, as
664 H3K4me3 and H3K27ac signals at their transcriptional start sites are similar in Normal and AD
665 conditions. The expression changes of paRNAs and paired promoter-sharing mRNAs displayed
666 poor correlation, too. This argues against that transcriptional/epigenetic deregulation is a main
667 reason for paRNA alteration in AD, as this otherwise should deregulate the promoter-sharing
668 gene mRNAs in a correlated manner. These results suggest a possibility that paRNA
669 deregulation in AD may happen at the post-transcriptional level, likely as a consequence of
670 defective RNA processing. Consistent with this, chemical inhibition of m6A reduces the stability
671 of *MAPT-paRNA* from a key AD locus (i.e., *MAPT*), lending support that m6A methylation acts
672 as at least one of the mechanisms in AD that can impact paRNA expression via stability control.

673 ***MAPT-paRNA* does not regulate neighboring *MAPT* mRNA or Tau protein levels**
674 Given the central role of Tau protein in the pathology of AD and other neurodegenerative
675 diseases, the locus coding Tau, *MAPT*, has been actively investigated to understand its mRNA
676 expression and translational control[75]. AD-associated genetic variants exist in this locus[76,77], and
677 ncRNAs are produced therein. It is important to discover AD-associated ncRNAs that can
678 regulate *MAPT*/Tau expression, which may offer mechanistic insights into Tauopathy in AD and
679 potentially new therapeutic avenues. Simone et al. reported that natural antisense transcripts
680 (named NAT in their work), which is essentially *MAPT-paRNA*, can play a role to suppress
681 *MAPT* mRNA translation[33], but this result was not agreed upon by another study[34]. In our work,
682 we found that *MAPT-paRNA* displayed much higher expression in iPSC-derived i3Neurons than
683 cell lines or other types of iPSC-derived brain cells, and it reached a stable expression in
684 morphologically mature excitatory neurons (i.e., with more than 5 weeks *in vitro* differentiation).
685 We considered i3Neurons to be a more relevant model for studying functions of this and other
686 brain paRNAs. Our knockdown of *MAPT-paRNA* did not impact *MAPT* expression either at
687 transcriptional or protein levels. This result was also consistent in SH-5YSY, a neuroblastoma
688 cell line model that displays low levels of *MAPT-paRNA*. In addition to the knockdown results,
689 the poor correlation between paRNA/mRNA changes in AD also supports that if paRNAs bear
690 functional roles, they unlikely regulate the genes directly adjacent to them. Furthermore, during
691 m6A/METTL3 inhibitor treatment (STM2457), while *MAPT-paRNA* expression was reduced,
692 the neighboring *MAPT* mRNA did not change. Together, our data are in agreement with a
693 conclusion that *MAPT-paRNA* does not regulate the neighboring *MAPT* expression or translation.
694
695 ***MAPT-paRNA* acts as a global regulator of neuronal/synaptic gene expression and protects**
696 **neuronal survival**
697 Instead of regulating the neighboring *MAPT* gene, we found that *MAPT-paRNA* knockdown in
698 mature i3Neurons altered around 200 genes, including both genes on the same chromosome and
699 a large majority on other chromosomes. This indicates that *MAPT-paRNA* plays a regulatory role
700 both *in cis* and *in trans*. By integrative analysis of the target genes and RNA-DNA interactome
701 data in the human brain offered by the MUSIC dataset[59], we found that the function of *MAPT-*
702 *paRNA* can be explained by its direct interaction with target genes in the 3D nucleus of
703 excitatory neurons. Interestingly, from MUSIC as well as snRNA-seq data, m6A-modified

704 paRNAs are more detectable. Also, m6A-modified paRNAs tend to display more target genes
705 and stronger contact strength with their target genes. These together support a positive
706 correlation between m6A and paRNA stability/functionality. In addition to *MAPT-paRNA*, our
707 analysis also found that cell-type-specific paRNAs in neurons often contact important
708 neuronal/synaptic genes. Many AD-deregulated paRNAs in Ex neurons can contact synaptic
709 genes more than background levels. These results indicate that many paRNAs may play roles in
710 cell-type-specific gene regulation in human brains. Distinct from the past work that often found
711 expression of paRNAs positively correlates with[23-26], and in some cases functionally impacts, the
712 expression of the neighboring gene sharing a promoter[27,28], our current findings offer a renewed
713 understanding of paRNAs as global regulators of gene expression *in cis* and *in trans*.
714
715 It is interesting that despite that many paRNAs can contact the same DNA loci (e.g., *MEF2C*),
716 knockdown of a single *MAPT-paRNA* can already cause obvious change of *MEF2C*
717 transcription. We found that in MUSIC data these paRNAs mostly engage with the target DNA
718 alone, i.e., there are rarely any molecular complexes that contain more than one paRNA (data not
719 shown). It is unknown how many of the 31 paRNAs that interact with *MEF2C* loci in Fig. 5H
720 can play a functional role in augmenting *MEF2C* transcription - it could be a few, and some
721 could even suppress *MEF2C* transcription. It is noteworthy that *MAPT-paRNA* may also impact
722 the transcription of these other paRNAs, which we noticed in i3Neurons with *MAPT-paRNA*
723 knockdown. We speculate that the *MAPT-paRNA* inhibition results in a collateral damage to a
724 putative "paRNA network" that could reduce the transcription of *MEF2C* gene from two layers:
725 1), directly from the loss of *MAPT-paRNA*; 2) indirectly from other paRNAs that are affected by
726 *MAPT-paRNA* loss. RNA transcription is being increasingly appreciated to take place in bursts[78].
727 We propose that many paRNAs are produced in dynamic transcriptional bursts, and they act via
728 dynamic interaction with target gene DNAs to achieve transcriptional regulation, potentially in a
729 collaborative manner.
730
731 As *MAPT-paRNA* showed increased expression in AD, we further explored its relevance to AD
732 disease etiology. A glutamate-induced neuronal excitotoxicity assay showed that *MAPT-paRNA*
733 plays a protective role under these conditions, which can be at least partially explained by its
734 positive regulation of key synaptic regulators such as MEF2C and SYNGAP1. Similar protective

735 role of this paRNA was found when neurons were challenged with Aβ-42 directly, one of the
736 most known neuronal stresses in AD. We are tempted to speculate that *MAPT-paRNA* and
737 perhaps some other regulatory paRNAs are upregulated in AD brains to safeguard key
738 synapse/neuronal gene expression so as to rectify the declining neuronal functions. However, the
739 full mechanisms underlying such paRNA regulation in human AD brains remain to be
740 determined at this stage. Future research is warranted to dissect the cause of paRNA deregulation
741 in AD, as well as the detailed mechanisms as to how individual paRNAs can regulate target
742 genes in a 3D nucleus.
743
744 **Limitations of the current study**
745 We utilized six brain samples from NCI and AD donors in this study, which in our knowledge,
746 represented one of the largest that studied total RNA m6A methylome in human brains from
747 normal/AD. However, this number remains limited, and some of the differential m6A sites
748 revealed by current work will need additional larger datasets to be fully validated. Future work
749 may also aim to profile RNA m6A methylome from multiple brain regions and/or from purified
750 individual brain cell types to achieve higher temporal and spatial resolution. In this work we
751 employed the MUSIC data to study RNA-DNA interactomes of paRNAs to understand the
752 mechanisms of their action in gene regulation, but we observed that the detectability of paRNAs
753 in MUSIC[59] is lower than that of snRNA-seq data[52]. For example, about 10-20% of Ex neurons
754 in snRNA-seq can detect *MAPT-paRNA* expression but this number ranges from one to a few
755 percent in MUSIC. Therefore, the target gene numbers and DNA contact strengths of paRNAs
756 seen in MUSIC may represent an under-estimation, and the paRNA-DNA interactome changes
757 in AD cannot be confidently calculated at this stage. In addition, regarding the role of m6A, we
758 noted that the change of *MAPT-paRNA* expression appeared to be quantitative after m6A
759 inhibition (by either chemical or genetic approaches). This suggests that m6A is likely one of the
760 mechanisms, rather than the only, that can impact *MAPT-paRNA* expression in human brains.
761
762 In summary, our results provided a blueprint of the m6A methylome in human brain and AD
763 disease, particularly on various ncRNAs. We reveal previously unknown roles of paRNAs, as
764 exemplified by *MAPT-paRNA,* as global transcriptional regulators in human neurons via

765 navigating 3D nuclear organization, offering new insights into the epitranscriptome regulation of
766 brain gene expression, neuronal survival, and AD pathogenesis.

767 **Methods**

768 **Human brain sample collection**

769 Together with Dr. Hui Zheng (Baylor College of Medicine), we collected RNAs from the middle
770 frontal cortex (FC) of 12 Normal and AD patients (**Supplementary Table 1**). Paired total RNA-
771 seq and m6A RNA methylome (m6A RIP-seq) data were generated from these samples. These
772 tissues were originally collected by the Center for Neurodegenerative Disease Research (CNDR)
773 from University of Pennsylvania and were provided to Dr. Hui Zheng.

774

775 **Cell culture**

776 H1-hESCs (WA01) and WTC11 iPSCs were purchased from WiCell and Coriell, respectively.
777 WTC11-Ngn2 iPSCs with doxycycline-inducible Ngn2 expression cassette was generously
778 provided by Drs. Li Gan[54] and Yin Shen (UCSF). Both iPSCs and ESCs were maintained in
779 mTeSR1 medium (Stemcell Technologies) on Matrigel-coated plates (Corning, 354230) with
780 daily medium replacement. We followed NIH 4D nucleome standard protocol for cell
781 maintenance. HMC3 and SH-SY5Y were purchased from ATCC and were cultured in
782 DMEM/F12 supplemented with 10% fetal bovine serum (FBS).

783

784 **Differentiation of H1-hESCs to NPCs and astrocytes**

785 H1-hESCs derived NPCs and astrocytes were generated according to a previous report[79]. In
786 brief, hESCs were dissociated into single cells and cultured in AggreWell 800 plates (Stemcell
787 Technologies, 34811) to form embryoid bodies (EBs) in Neural Induction Medium (Stemcell
788 Technologies). On day 5, EBs were collected and transferred to 6-well plates coated with
789 Matrigel for culture in the NPC medium. Neural rosettes were collected and dissociated into
790 single cells using Neural Rosette Selection Reagent (StemCell Technologies, 05832) after 14
791 days of culture. The hESCs-derived NPCs were then cultured in Neural Progenitor Medium
792 (Stemcell Technologies, 05833), and passaged every 4-5 days. Following validation by
793 immunostaining with NPC markers, the cells were cryopreserved in liquid nitrogen for future
794 usage. For the differentiation of NPCs into astrocytes, NPCs were dissociated into single cells
795 using accutase (Thermo Fisher, 00-4555-56) and plated on Matrigel-coated plates in astrocyte
796 medium (ScienCell Research Laboratories, 1801) for 20 days, followed by splitting and

797 subculturing until day 75. After validation by immunostaining with astrocyte markers, the cells
798 were frozen for future analysis.
799
800 **Differentiation of WTC11 iPSCs to microglia**

801 iPSC-derived microglia were generated following established protocols with some
802 modifications[80,81]. In brief, iPSCs were cultured in mTeSR plus medium (Stemcell Technologies)
803 on Matrigel-coated plates with daily medium replacement. The cells were dissociated into single
804 cells using accutase and cultured in a 96-well ultra-low attachment plate (Corning, 7201680) to
805 form yolk-sac embryoid bodies (YS-EBs) in 100 µL YS-EBs medium (10 mM ROCK inhibitor,
806 50 ng ml-1 BMP-4, 20 ng ml-1 SCF, and 50 ng ml-1 VEGF-121 in mTeSR plus), with 10,000
807 cells per well on Day 0. The culture medium was replaced on Days 2 and 4 with fresh YS-EBs
808 medium without ROCK inhibitor. On Day 5, the YS-EBs were transferred to a 6-well plate with
809 10-12 YS-EBs per well and incubated in 3 mL hematopoietic medium (2 mM GlutaMax, 100 U
810 ml-1 penicillin, 100 mg ml-1 streptomycin, 55 mM β-mercaptoethanol, 100 ng ml-1 M-CSF, and
811 25 ng ml-1 IL-3 in X-VIVO 15) to induce the generation of primitive macrophage precursors
812 (PMPs). The medium (2 mL) was replaced with fresh hematopoietic medium every 5 days, and
813 PMPs typically emerged as rounded brilliant cells in suspension within 2 weeks. Subsequently,
814 PMPs were harvested from suspension and cultured on Matrigel-coated 6-well plates in
815 microglia medium (DMEM/F12, 2X insulin-transferrin-selenium, 2X B27, 0.5X N2, 1X
816 GlutaMax, 1X non-essential amino acids, 400 µM monothioglycerol, 5 µg ml-1 insulin)
817 supplemented with three protein factors (100 ng ml-1 IL-34, 50 ng ml-1 TGFβ1, and 25 ng ml-1
818 M-CSF) for 25 days, with half-medium replacement every 3 days. After 25 days of culture, the
819 cells were further incubated in microglia medium supplemented with five protein factors (100 ng
820 ml-1 IL-34, 50 ng ml-1 TGFβ1, 25 ng ml-1 M-CSF, 100 ng ml-1 CD200, and 100 ng ml-1
821 CX3CL1) for an additional 3 days to achieve further maturation. Following validation through
822 immunostaining with microglial markers, the iPSC-derived microglia were ready for subsequent
823 treatment or analysis.
824
825 **i3Neuron differentiation**

826 WTC11-Ngn2 iPSCs were utilized to generate i3Neurons following a previously established
827 protocol [52]. For pre-differentiation, WTC11-Ngn2 iPSCs were cultured with 2 µg ml-1

828 doxycycline in knockout DMEM/F12 medium supplemented with 1× N2, 1× NEAA, 1 μg ml−1
829 mouse laminin, 10 ng ml−1 brain-derived neurotrophic factor (BDNF) and 10 ng ml−1 NT3 for
830 three days. ROCK inhibitor (10 μM) was included in the predifferentiation media for the first
831 day, and the medium was replaced daily. During the maturation phase, predifferentiated neural
832 cells were dissociated into single cells using accutase and plated on Poly-L-Ornithine-coated
833 plates in maturation medium containing equal parts DMEM/F12 and Neurobasal-A with
834 2 μg ml−1 doxycycline, 0.5× B-27, 0.5× N-2, 1× NEAA, 0.5× GlutaMax, 1 μg ml−1 mouse
835 laminin, 10 ng ml−1 BDNF and 10 ng ml−1 NT3. Doxycycline was only added to the maturation
836 medium on the first day and omitted thereafter. Half of the medium was replaced weekly for the
837 first 2 weeks, and the medium volume was doubled on week 3. Subsequently, one third of the
838 medium was replaced weekly until 8 weeks for further treatment.
839
840 ***MAPT-paRNA* stability measurement**
841 To study the effect of m6A methylation on *MAPT-paRNA* stability, 8-week-old i3Neurons were
842 treated with m6A/METTL3 inhibitor STM2457 (10 μM, MedChemExpress, HY-134836) or
843 DMSO vehicle for 24 hours. Following this treatment, Flavopiridol (2 μM, Sigma, F3055) was
844 added to inhibit transcriptional activity. The RNA levels of *MAPT-paRNA* were then measured at
845 various time points after transcriptional inhibition using RT-qPCR.
846
847 **Antisense oligonucleotides (ASOs)-based Knockdown**
848 Knockdown experiments were performed using antisense oligonucleotides (ASOs) with
849 modifications by the Affinity Plus nucleic acid modification (IDT) (**see Supplementary Table**
850 **9**). A sequence-scrambled ASO (Scr ASO) was used as a control. ASOs was dissolved in TE
851 buffer (10 mM Tris-HCl, pH 7.4, 1 mM EDTA) and directly added to the i3Neuron culture
852 without any transfection reagent (termed gymnosis) at a final concentration of 10μM. After 3
853 days of ASOs treatment (unless otherwise indicated), cells were harvested for downstream
854 analysis.
855
856 **Western blotting analysis**
857 Cells were washed twice with cold PBS buffer and subsequently lysed in RIPA buffer (50 mM
858 Tris, pH 7.4, 150 mM NaCl, 1 mM EDTA, 0.1% SDS, 1% NP-40, 0.5% sodium deoxycholate)

859 containing cOmplete Mini Protease Inhibitor Cocktail (Roche, 11836153001) on ice for 30
860 minutes. Following centrifugation at 12,000 × g for 10 minutes at 4°C, the supernatants were
861 combined with 2x Laemmli sample buffer (Bio-Rad, 1610737) and boiled at 95 °C for 10
862 minutes. The protein samples were loaded and separated using 4%–15% SDS–PAGE gradient
863 gels, then transferred to a PVDF membrane (Bio-Rad, 1620260). Subsequently, the membranes
864 were blocked in 5% skim milk in TBST (20 mM Tris, 150 mM NaCl, and 0.2% Tween-20, w/v)
865 for 1 hour and incubated with primary antibodies, anti-SYNGAP1 (1:2000; CST; #62193S), anti-
866 MEF2C (1:1000; Abcam; #ab211493), anti-HDAC4 (1:2000; CST; #7628T), anti-Synapsin1
867 (1:1000; SYSY; #106011), anti-PSD95 (1:1000; Sigma; #MAB1596), anti-GluN1 (1:1000;
868 SYSY; #114011), anti-GluA2 (1:1000; BioLegend; #810501), anti-Total Tau (1:20000; Dako;
869 #A0024), anti-pTau (Ser202/Thr205) (1:1000; Thermo Fisher; #MN1020), anti-Tubulin (1:5000;
870 Thermo Fisher; #A11126), or anti-GAPDH (1:50000; Proteintech; #60004). After three washes
871 in TBST, the membranes were incubated with horse-radish peroxidase (HRP)-conjugated
872 secondary antibody for 1 hour. Following six washes, protein bands were visualized using the
873 Enhanced Chemiluminescence kit (Pierce) and developed in the Bio-Rad ChemiDoc gel imaging
874 system. Band intensities were quantified using ImageJ software, with tubulin blots serving as
875 loading controls.
876
877 **Glutamate-induced neuronal excitotoxicity assay**
878 To investigate the neuroprotective role of *MAPT-paRNA*, we implemented glutamate-induced
879 excitotoxicity based on established protocols with slight modifications[74,82]. In detail, i3Neurons
880 were cultured and differentiated in a 24-well plate for 8 weeks and treated with Scr ASO or
881 MAPT-paRNA-ASO1 for 3 days. Subsequently, vehicle or 10μM L-glutamate (Sigma, G1251)
882 was introduced into the medium for 2 hours. Then the cells were stained with Hoechst 33342
883 (5 μg ml−1) (Thermo Fisher, 62249) and propidium iodide (PI, 1 μg ml−1) (Thermo Fisher,
884 P21493) for 30 min to visualize total and dead cells, respectively. Images were captured using a
885 Keyence BZ-X810 Fluorescence Microscope, and neurons from at least 3 wells were quantified.
886 To assess the toxicity of ASOs alone on i3Neurons, the same protocol was applied, excluding the
887 L-glutamate treatment.

888 **Beta-amyloid (Aβ-42)-induced cytotoxicity**

889 To assess the role of MAPT-paRNA under Aβ-induced stress, 8-week-cultured i3Neurons were
890 treated with either Scr ASO or MAPT-paRNA-ASO1 in the presence of scrambled beta-amyloid
891 (Scr Aβ-42, Anaspec, #AS-25382) or beta-amyloid (Aβ-42, Anaspec, #AS-64129-05) for six
892 consecutive days. Cell cytotoxicity was evaluated daily by measuring lactate dehydrogenase
893 (LDH) levels in the culture media using the LDH Assay Kit (Sigma, #MAK066).

894 **Electrophysiological recordings**

895 Electrophysiological recordings were conducted at room temperature using 8-week-cultured
896 i3Neurons in a whole-cell patch-clamp configuration. Patch pipettes with a resistance of 8–15
897 MΩ were filled with an internal solution containing 135 mM CsF, 33 mM CsCl, 2 mM $MgCl_2$, 1
898 mM $CaCl_2$, 11 mM EGTA, and 10 mM HEPES (pH 7.4). The external ACSF solution consisted
899 of 140 mM NaCl, 7 mM KCl, 2 mM $CaCl_2$, 10 mM HEPES, 10 mM glucose, 10 μM bicuculline,
900 and 1 mM TTX (pH 7.4). To selectively study NMDA receptor-mediated currents with
901 glutamate, non-NMDA receptors were blocked using 10 μM NBQX. Conversely, for
902 investigating AMPA receptor-mediated currents, NMDA receptors were blocked with 100 μM
903 APV and 25 μM DCKA. External solutions were locally applied to neurons using an SF-77B
904 Fast-Step perfusion system (Warner Instruments). All recordings were performed at room
905 temperature with a holding potential of −60 mV using an Axopatch 200B amplifier (Molecular
906 Devices). Data were acquired at 10 kHz using pCLAMP10.7 software (Molecular Devices) and
907 filtered online at 5 kHz. Current densities were calculated by dividing the recorded current (pA)
908 by the measured cell membrane capacitance (pF).

909 **Immunocytochemistry**

910 For immunofluorescence immunostaining, the cells were cultured on coverslips, then washed
911 twice with PBS and fixed in cold methanol (-20°C) for 15 min. Subsequently, the cells were
912 permeabilized and blocked with PBS containing 5% goat serum, 5% BSA (bovine serum
913 albumin), and 0.3% Triton X-100 for 1 h, followed by incubation with primary antibodies diluted
914 in blocking buffer overnight at 4°C. After incubation with fluorescence-conjugated secondary
915 antibodies at room temperature for 1 hour, cell nuclei were counterstained with DAPI, and
916 images were acquired using a confocal microscope (Nikon A1) or fluorescence microscope
917 (Keyence). Antibodies used for immunocytochemistry were against PSD95 (1:200; Sigma;
918 #MAB1596), GluN1 (1:200; SYSY; #114011), NeuN (1:200; ThermoFisher; #702022), and

919 MAP2 (1:400; Abcam; #ab5392). To quantify the intensity of immunostaining images, ImageJ
920 software (ImageJ website: http://imagej.nih.gov.laneproxy.stanford.edu/ij/) was used. A
921 minimum of 15 neurons from 3 separate experiments were quantified for statistical analysis.
922
923 **Quantitative RT-PCR (qRT-PCR)**
924 Total cellular RNAs were extracted by TRIzol (Thermo Fisher) or Zymo RNA miniprep kit
925 (Zymo Research), following the respective manufacturer's instructions. The extracted RNA
926 underwent reverse transcription by SuperScript IV (Thermo Fisher) for first strand cDNA
927 synthesis using random hexamer. For qPCR, the SsoAdvanced Universal SYBR green Supermix
928 (Bio-Rad) was used according to the standard parameters recommended by the manufacturer.
929 Primer sequences were shown in **Supplementary Table 9**. All qPCR analyses were performed
930 in triplicate, and each value was denoted by a black dot.
931
932 **RNA-seq, MeRIP-seq, and MeRIP-qPCR**
933 RNA-seq and MeRIP-seq were performed according to our previous report with some
934 modifications [12]. Total RNA (2-5 μg) was fragmented at 70 °C for 6 min in the fragmentation
935 buffer (10 mM ZnCl2, 10 mM TrisHCl pH7.4), following precipitation the RNA was
936 resuspended with ice-cold IP buffer (10 mM Tris-HCl, pH 7.4, 150 mM NaCl, 0.1% NP-40, 20
937 U/mL Superase-In, 1× Protease Inhibitor) to a final volume of 1050 μL. Of this, 50 μL of diluted
938 RNA was utilized for RNA-seq (5% input for m6A IP) and the remaining 1000 μL was reserved
939 for MeRIP-seq (Methylated RNA immunoprecipitation sequencing). To prepare anti-m6A
940 antibody conjugated beads, 20 μL of Dynabeads Protein G beads (Thermo Fisher) was washed 3
941 times with 1ml IP buffer and then incubated with 1 μg of m6A antibody (Synaptic Systems, #
942 202003) at room temperature for 30min. The conjugated anti-m6A-Dynabeads were washed in
943 1ml IP buffer 3 times. Subsequently, the RNA sample was mixed with the beads and rotated at
944 4 °C for 3 hours. The beads were then washed in the IP buffer 5 times. The immunoprecipitated
945 RNAs were extracted from the beads by TRIzol-LS (Thermo Fisher). The extracted RNA was
946 subjected to the next generation sequencing library preparation for RNA-seq and MeRIP-seq, as
947 well as qPCR, to quantify the m6A levels.
948
949 **Library Preparation and Sequencing**

950 RNA samples were collected by one of two methods: lysis in TRIzol reagent (Thermo Fisher) for
951 RNA-seq and MeRIP-seq, followed by standard phenol-chloroform extraction methods; or
952 alternatively, lysis was performed using Zymo Research Quick-RNA MiniPrep kit (Genesee
953 Scientific) for regular qPCR following the manufacturer protocol. Libraries for RNA-Seq and
954 MeRIP-Seq were made with NEBNext Ultra II Directional Library Prep Kit for Illumina (NEB,
955 #E7760) following the manufacturer's instructions. Ribosome RNA was depleted with NEBNext
956 rRNA Depletion Kit (NEB, #E6301S). The generated libraries were quantified using the Qubit-3
957 system and/or qPCR. Sequencing of the libraries was performed using a NextSeq 550 platform
958 (Illumina) with paired-end sequencing (40/40nt mode).
959
960 **RNA-seq data analysis**
961 We used FastQC (v.0.11.8) (https://www.bioinformatics.babraham.ac.uk/projects/fastqc/) to
962 check the quality of RNA-seq raw reads. RNA-seq clean reads were aligned to the human
963 reference genome (hg19) or mouse reference genome (m31) from the UCSC database using
964 HISAT2 (v.2.2.1)[83] with *-k 1 --no-discordant --rna-strandness RF*. StringTie (v.2.1.6)[84] was
965 implemented to assemble and quantify transcripts based on gencode.v19.annotation.gtf (human)
966 or gencode.vM31.annotation.gtf (mouse). DESeq2 (v.1.34.0)[85] was run to analyze differentially
967 expressed genes (DEGs). DEGs between AD and Normal groups were defined based on *p.adj* <
968 0.05 and absolute $\log_2$foldchange > 1. Differentially expressed paRNAs between Normal and
969 AD/ALS/PD/FTD brains were selected based on *p.adj* < 0.05 and absolute $\log_2$foldchange >
970 log2(1.5). For *MAPT-paRNA* control and KD RNA-seq data, DEGs were defined based on *p.adj*
971 < 0.05 and absolute $\log_2$foldchange > log2(1.5).
972
973 **ChIP-seq analysis**
974 We firstly downloaded Non Cognitive Impairment (NCI) and AD H3K27ac and H3K4me3
975 ChIP-seq fastq files from ENCODE (https://www.encodeproject.org/brain-
976 matrix/?type=Experiment&status=released&internal_tags=RushAD) and H3K27ac ChIP-seq
977 data (GSE153875) (Nativio et al. [36]). We used FastQC (v.0.11.8)
978 (https://www.bioinformatics.babraham.ac.uk/projects/fastqc/) to check the quality of ChIP-seq
979 reads. We applied Bowtie2 (v.2.2.5)[86] with --very-sensitive to map clean reads from ChIP-seq to
980 hg19 from the UCSC database, and duplicates are further removed with picard. MACS3

981 (v.3.0.0a6)[39] (https://github.com/macs3-project/MACS) was used to call H3K27ac and
982 H3K4me3 peaks, respectively.
983
984 ***De novo transcript calling***
985 We followed the previous method[42,43] to identify RNA transcripts using STAN R package
986 (v.2.22.0)[87]. Briefly, we merged the bam files from the same group to increase the sequencing
987 depth, and convert the bam to bed files. Next, we applied the STAN package to the bed file with
988 default parameters. To define paRNAs, the transcription start sites (TSSs) of any possible
989 paRNAs overlapping with the promoter regions (-2kb to 2kb) of genes were retained.
990
991 **Long-reads Nanopore Direct RNA-seq data Analysis**
992 We downloaded the long-reads RNA-seq datasets from ENCODE
993 (https://www.encodeproject.org/brain-
994 matrix/?type=Experiment&status=released&internal_tags=RushAD). We followed the ENCODE
995 pipeline to reanalyze long-read RNA-seq datasets. Here we used minimap2 (v.2.17-r941)[88] to
996 map the long-read RNA-seq data to the hg19 genome build. Next, TALON (v5.0)[89] was used to
997 quantify the expression of transcripts. Any lincRNA, antisense RNA, processed_transcript or
998 unannotated transcripts overlapping with the transcription start sites (TSSs) of PCGs were
999 retained.
1000
1001 **MeRIP-seq data analysis**
1002 Similar to RNA-seq data analysis, we used the same pipeline to map clean MeRIP-seq data to the
1003 human reference genome. We used MACS3 (v.3.0.0a6)[39] (https://github.com/macs3-
1004 project/MACS) with --nomodel --extsize 100 to call m6A peaks.The high-confidence m6A peaks
1005 were retained based on q value $\leq 10^{-5}$ and fold change ≥ 5. We used bedtools (v.2.30.0)[90] to get
1006 intersected m6A peaks detected in at least 3 samples. We used ChIPseeker (v.1.40.0)[91] to
1007 annotate the genomic region of a m6A peak as TSS, exon, 5′ UTR, 3′ UTR, intronic or
1008 intergenic. The 'gencode.v19.annotation.gtf' was used as the transcript database. Gene promoter
1009 regions were defined on the basis of -2 kb distance from TSS. For m6A peaks annotated to
1010 ncRNAs, we used m6A peaks to overlap with ncRNAs identified by *de novo* calling or repetitive
1011 elements downloaded from UCSC Genome Browser.

1012 **Differential analysis of m6A peaks**

1013 The gained or lost m6A peaks were determined by whether the genomic coordinates of any m6A
1014 peaks overlap or not. Of note, this criterion is markedly biased by the peak calling algorithm. For
1015 example, the enrichment fold of a genomic region is 4.9 and 5.1 in Normal and AD brains,
1016 respectively. Thus, this genomic region would have a m6A peak in AD, but not in Normal
1017 brains. Moreover, the difference in m6A ratio (MeRIP/input) in this genomic region between
1018 Normal and AD brains was not large. The existing algorithms analyzing differential m6A peaks
1019 divided the genomic regions into different bin sizes and compared the differences in m6A ratio
1020 between case and control samples. These algorithms have at least 3 limitations. First of all, there
1021 is no gold standard for choosing a proper bin size. In addition, continuous bin sizes have
1022 significant differences in m6A ratio, these continuous bin sizes would be concatenated, which
1023 would make a m6A peak region large. Third, the genomic coordinates of these differential m6A
1024 peaks called by the existing algorithms do not match the genomic coordinates of m6A peaks
1025 called by MACS3. To address these questions, we merged the m6A peaks from Normal and AD
1026 brains to obtain unique m6A peaks, and then calculated the RNA (referred to as *raw*
1027 *FPKM(RNA)*) and m6A methylation (referred to as *raw FPKM(m6A)*) levels for each m6A peak
1028 region. Given the sparsity of RNAs in some m6A peak regions, we added a pseudocount of the
1029 first quantile of RNA levels from each input sample to *raw FPKM(RNA)* to get the *final*
1030 *FPKM(RNA)*, and calculated the m6A ratio based on the *raw FPKM(m6A)* divided by *the final*
1031 *FPKM(RNA)*. Here is the formula for the normalized m6A ratio:
1032 $\frac{FPKM(MeRIP)}{FPKM(Input)+pseudoCount}$. We further removed the outliers of m6A ratio less than 3.5 based on the
1033 quantile distributions of m6A ratio. Next, we performed the paired student's t test for m6A ratio
1034 of each m6A peak between AD and Normal brains. We selected the differential m6A peaks
1035 based on the fold change > 1.5 and $p < 0.1$.

1036

1037 **Gene Ontology analysis**

1038 We applied gProfiler2 (v.0.2.2)[92] to analyze the functional enrichment of genes. Significant GO
1039 terms will be selected based on a 5% false discovery rate (FDR).

1040

1041 **snRNA-seq data analysis**

1042 We downloaded control and Alzheimer's disease snRNA-seq datasets[52]. Based on the previous
1043 method[93], we used the cellranger count (v.7.0.0)[94] with default parameters to align the snRNA-
1044 seq data to the hg19 human reference genome including mRNAs and paRNAs to produce the
1045 raw cell-by-gene count matrix based on the barcode matrix for all snRNA-seq libraries. Next, we
1046 used Seurat (v.5.0.0)[95] to filter out low quality nuclei based on nFeature_RNA > 200 &
1047 nFeature_RNA < 10000 & percent.mt < 5. Subsequently, the merged expression matrix was
1048 normalized by the NormalizeData with default parameters from Seurat. The principal
1049 components were calculated using the first 3000 variable genes, and the Uniform Manifold
1050 Approximation and Projection (UMAP) analysis was performed with RunUMAP from Seurat.
1051 The FindAllMarkers from Seurat was used to analyze the differentially expressed genes across
1052 different clusters. Finally, we used the previously identified marker genes[52] to define the
1053 different cell clusters or cell types. Here if a paRNA was detected in more than 3% cells of a
1054 given cell type, then that paRNA was defined as a detected paRNA in that cell type in snRNA-
1055 seq data.
1056
1057 **MUSIC data analysis**
1058 To analyze how many paRNAs are detected by MUSIC data, we directly used the processed
1059 reads/cells/complex matrix reported in Wen et al.[59], (which is in hg38 genome build). We
1060 liftovered the genomic coordinates of our paRNAs from hg19 genome to hg38, and intersected
1061 the genomic coordinates of paRNAs we identified in human brain bulk RNA-seq datasets with
1062 the RNA reads from MUSIC data. Here if a paRNA was detected in more than 3% cells of a
1063 given cell type based on the cell barcoder (CB), then that paRNA was defined as a detected
1064 paRNA in that cell type in MUSIC data. The expression pattern of paRNAs is similar when
1065 using a more stringent cutoff (e.g., 5% of cells expressing paRNAs). To identify the target genes
1066 of paRNAs of interest, the DNA reads interacting with paRNAs were identified based on shared
1067 cell barcodes and molecular barcodes (CBMB) between RNA reads and DNA reads. To annotate
1068 these DNA reads to genes, we used the gene body to overlap with the DNA reads interacting
1069 with paRNAs. To remove technical issues, we remove large molecular complexes with RNA
1070 reads>50 and DNA reads>1000. We followed the method described by Wen et al.[59] to calculate
1071 the contact strength between RNA reads and DNA reads in a complex: $\frac{M * N}{M + N}$, M and N represent
1072 the number of RNA reads and DNA reads in a complex, respectively. Synaptic genes (n=393)

1073 were extracted from **Supplementary Fig, 11C**, and then we calculated the contact strength
1074 between AD-deregulated paRNAs (DE paRNAs, n = 47) / non-AD-deregulated paRNAs (n =
1075 346) and these synaptic genes (n=393).
1076
1077 **Motif analysis**
1078 We ran Homer (findMotifsGenome -rna -len 5,6,7)[96] to analyze m6A peaks and to identify m6A
1079 motifs.
1080
1081 **Quantification and statistical analysis**
1082 All bar graphs of qPCR data were presented as mean ± SD as indicated in figure legend using
1083 Prism 6.0. Two-tailed Student's t-test was used to compare means between groups as indicated; p
1084 < 0.05 was considered significant, and p values with asterisks are indicated in each figure panel.
1085 $*$, $p < 0.05$; $**$, $p < 0.01$; $***p < 0.001$. Statistical details of experiments can be found in the
1086 figure legends. No statistical methods were used to pre-determine sample sizes. For all boxplots,
1087 the central lines represent medians; box limits indicate the 25th and 75th percentiles; and
1088 whiskers extend 1.5 times the interquartile range (IQR) from the 25th and 75th percentiles. For
1089 NGS data analysis, statistical analysis was performed using Python (v.3.8) and R (v.4.3), and is
1090 indicated in the legend of each figure panel.
1091
1092 **Acknowledgments**
1093 This work was supported the University of Texas UTHealth McGovern Medical School at
1094 Houston Startup fund, NIH/NIA (R01AG082132), the '4D Nucleome' program
1095 (U01HL156059), NIGMS (R01GM136922), Cancer Prevention and Research Institute of Texas
1096 (CPRIT, RR160083), and Welch foundation (AU-2000-20220331) to W.L.; by NIH grant
1097 U01DA052769 to X.X.; by NIH/NCI (R01CA246130), NIH/NHLBI (R01HL142704), and
1098 CPRIT(RR160019) to D.-F.L.; by grants from '4D Nucleome' program (U01CA200147),
1099 NIGMS (R01GM138852), NIDDK (DP1DK126138), NICHD (R01HD107206), and a Kruger
1100 research grant to S.Z.; by grants from NIH RF1 AG020670, RF1 NS093652, and P01 AG066606
1101 to Z.H.; by NIGMS R35GM122528 to V.J., and by NIAID P01AI077774-S and NIA
1102 RF1AG059321 to C.S.. B.H. was partially supported by the CPRIT Biomedical Informatics,
1103 Genomics and Translational Cancer Research Training Program (BIG-TCR) postdoctoral

fellowship (RP210045). Our next generation sequencing work was mostly conducted with the UTHealth Cancer Genomics Core, which received funding from CPRIT (RP240610). We thank WiCell and Coriell for hESCs and iPSCs, and thank Drs. Li Gan (Weill Cornell) and Yin Shen (UCSF) for generously sharing the WTC11-ngn2 cell model. We are grateful to the donors who contributed samples and knowledge to the ENCODE, RUSH program and AD Knowledge Portal and for kindly sharing these datasets with the scientific community.

Author contributions

W.L., B.H., and Y.S. conceived the project. B.H. conducted all the dry lab experiments. Y.S. did most of the wet lab experiments, with help from Y.-T.C., X.Z. and N.D. F.X. generated the original RNA-Seq and MeRIP-Seq datasets. H.Z. and R.C. acquired human brain tissues and contributed to i3Neuron work, and D.-F.L. and C.S. helped on neuronal/glial cell differentiation and culture. X.W. and S.Z. shared and helped with MUSIC data. E.F. and V.J. contributed the electrophysiology results. W.L., B.H., and Y.S. wrote the manuscript, with inputs from all authors. These authors contributed equally: Benxia Hu, Yuqiang Shi.

Corresponding author

Correspondence to Wenbo Li (Wenbo.Li@uth.tmc.edu).

Declaration of interests

The authors declare no competing interests.

Data availability

Public data:

H3K4me3 and H3K27ac ChIP-seq, and RNA-seq datasets generated from No Cognitive Impairment and AD DLPFC are available through (https://www.encodeproject.org/brain-matrix/?type=Experiment&status=released&internal_tags=RushAD). Old and AD lateral temporal lobe RNA-seq datasets are available through GSE104704 (Nativio et al., PMID: 32989324), and H3K27ac ChIP-seq data are available through GSE153875 (Nativio et al., PMID: 29507413). RNA-seq data generated from the 5xFAD mice brain (right cerebral hemisphere) are available through https://www.synapse.org/#!Synapse:syn21983020. RNA-seq

data generated from the 3xTg-AD mouse mode are available through https://www.synapse.org/#!Synapse:syn22964719. RNA-seq data generated from the P301S mouse model are available through GSE226385 (Udeochu et al., PMID: 37095396). RNA-seq data generated from Parkinson's disease are available through GSE148434 (PD, Lee et al., PMID: 37058563), Frontotemporal Dementia are available through GSE116622 (FTD, Conlon et al., PMID: 30003873), and Amyotrophic lateral sclerosis are available through GSE124439 (ALS, Tam et al., PMID: 31665631). RNA-seq data from iPSC-derived cellular models are available through GSE102956 (Lin et al., Neuron, PMID:29861287). DLPFC Normal and AD snRNA-seq data are available through GSE174367 (Morabito et al., PMID:34239132).

Data generated by this work:
Data generated in this study have been deposited to NCBI GEO (GSE266459). The reviewer token is *mjidasquplmzbcx*. Source Data are provided with this paper (Source Data Files 1,2,3). Source data and codes in this paper are also available at Zenodo (https://doi.org/10.5281/zenodo.15019230)[97].

Code availability

All custom code used in this work is available in the following github repository:(https://github.com/BenxiaHu/MAPT-paRNA_in_AD). Genomic tracks are generated by the HiCPlot NGStrack function (https://github.com/BenxiaHu/HiCPlot).

1155 **Reference**

1156 1. 2023 Alzheimer's disease facts and figures. (2023). Alzheimers Dement *19*, 1598-1695.
1157 10.1002/alz.13016.
1158 2. Knopman, D.S., Amieva, H., Petersen, R.C., Chetelat, G., Holtzman, D.M., Hyman, B.T.,
1159 Nixon, R.A., and Jones, D.T. (2021). Alzheimer disease. Nat Rev Dis Primers *7*, 33.
1160 10.1038/s41572-021-00269-y.
1161 3. DeTure, M.A., and Dickson, D.W. (2019). The neuropathological diagnosis of
1162 Alzheimer's disease. Mol Neurodegener *14*, 32. 10.1186/s13024-019-0333-5.
1163 4. Nachtergaele, S., and He, C. (2018). Chemical Modifications in the Life of an mRNA
1164 Transcript. Annu Rev Genet *52*, 349-372. 10.1146/annurev-genet-120417-031522.
1165 5. Zaccara, S., Ries, R.J., and Jaffrey, S.R. (2019). Reading, writing and erasing mRNA
1166 methylation. Nat Rev Mol Cell Biol *20*, 608-624. 10.1038/s41580-019-0168-5.
1167 6. Alarcon, C.R., Goodarzi, H., Lee, H., Liu, X., Tavazoie, S., and Tavazoie, S.F. (2015).
1168 HNRNPA2B1 Is a Mediator of m(6)A-Dependent Nuclear RNA Processing Events. Cell
1169 *162*, 1299-1308. 10.1016/j.cell.2015.08.011.
1170 7. Liu, J., Dou, X., Chen, C., Chen, C., Liu, C., Xu, M.M., Zhao, S., Shen, B., Gao, Y., Han,
1171 D., and He, C. (2020). N (6)-methyladenosine of chromosome-associated regulatory
1172 RNA regulates chromatin state and transcription. Science *367*, 580-586.
1173 10.1126/science.aay6018.
1174 8. Patil, D.P., Chen, C.K., Pickering, B.F., Chow, A., Jackson, C., Guttman, M., and Jaffrey,
1175 S.R. (2016). m(6)A RNA methylation promotes XIST-mediated transcriptional
1176 repression. Nature *537*, 369-373. 10.1038/nature19342.
1177 9. Xiang, Y., Laurent, B., Hsu, C.H., Nachtergaele, S., Lu, Z., Sheng, W., Xu, C., Chen, H.,
1178 Ouyang, J., Wang, S., et al. (2017). RNA m(6)A methylation regulates the ultraviolet-
1179 induced DNA damage response. Nature *543*, 573-576. 10.1038/nature21671.
1180 10. Xu, W., Li, J., He, C., Wen, J., Ma, H., Rong, B., Diao, J., Wang, L., Wang, J., Wu, F., et
1181 al. (2021). METTL3 regulates heterochromatin in mouse embryonic stem cells. Nature
1182 *591*, 317-321. 10.1038/s41586-021-03210-1.
1183 11. Ruckle, C., Kortel, N., Basilicata, M.F., Busch, A., Zhou, Y., Hoch-Kraft, P., Tretow, K.,
1184 Kielisch, F., Bertin, M., Pradhan, M., et al. (2023). RNA stability controlled by m(6)A
1185 methylation contributes to X-to-autosome dosage compensation in mammals. Nat Struct
1186 Mol Biol *30*, 1207-1215. 10.1038/s41594-023-00997-7.
1187 12. Xiong, F., Wang, R., Lee, J.H., Li, S., Chen, S.F., Liao, Z., Hasani, L.A., Nguyen, P.T.,
1188 Zhu, X., Krakowiak, J., et al. (2021). RNA m(6)A modification orchestrates a LINE-1-
1189 host interaction that facilitates retrotransposition and contributes to long gene
1190 vulnerability. Cell Res *31*, 861-885. 10.1038/s41422-021-00515-8.
1191 13. Liu, J., Gao, M., He, J., Wu, K., Lin, S., Jin, L., Chen, Y., Liu, H., Shi, J., Wang, X., et al.
1192 (2021). The RNA m(6)A reader YTHDC1 silences retrotransposons and guards ES cell
1193 identity. Nature *591*, 322-326. 10.1038/s41586-021-03313-9.
1194 14. Chelmicki, T., Roger, E., Teissandier, A., Dura, M., Bonneville, L., Rucli, S., Dossin, F.,
1195 Fouassier, C., Lameiras, S., and Bourc'his, D. (2021). m(6)A RNA methylation regulates
1196 the fate of endogenous retroviruses. Nature *591*, 312-316. 10.1038/s41586-020-03135-1.
1197 15. Lee, J.H., Wang, R., Xiong, F., Krakowiak, J., Liao, Z., Nguyen, P.T., Moroz-Omori,
1198 E.V., Shao, J., Zhu, X., Bolt, M.J., et al. (2021). Enhancer RNA m6A methylation
1199 facilitates transcriptional condensate formation and gene activation. Mol Cell *81*, 3368-
1200 3385 e3369. 10.1016/j.molcel.2021.07.024.

1201 16. Liu, J., Li, K., Cai, J., Zhang, M., Zhang, X., Xiong, X., Meng, H., Xu, X., Huang, Z.,
1202 Peng, J., et al. (2020). Landscape and Regulation of m(6)A and m(6)Am Methylome
1203 across Human and Mouse Tissues. Mol Cell *77*, 426-440 e426.
1204 10.1016/j.molcel.2019.09.032.
1205 17. Yoon, K.J., Ringeling, F.R., Vissers, C., Jacob, F., Pokrass, M., Jimenez-Cyrus, D., Su,
1206 Y., Kim, N.S., Zhu, Y., Zheng, L., et al. (2017). Temporal Control of Mammalian
1207 Cortical Neurogenesis by m(6)A Methylation. Cell *171*, 877-889 e817.
1208 10.1016/j.cell.2017.09.003.
1209 18. Shi, H., Zhang, X., Weng, Y.L., Lu, Z., Liu, Y., Lu, Z., Li, J., Hao, P., Zhang, Y., Zhang,
1210 F., et al. (2018). m(6)A facilitates hippocampus-dependent learning and memory through
1211 YTHDF1. Nature *563*, 249-253. 10.1038/s41586-018-0666-1.
1212 19. Castro-Hernandez, R., Berulava, T., Metelova, M., Epple, R., Pena Centeno, T., Richter,
1213 J., Kaurani, L., Pradhan, R., Sakib, M.S., Burkhardt, S., et al. (2023). Conserved
1214 reduction of m(6)A RNA modifications during aging and neurodegeneration is linked to
1215 changes in synaptic transcripts. Proc Natl Acad Sci U S A *120*, e2204933120.
1216 10.1073/pnas.2204933120.
1217 20. Djebali, S., Davis, C.A., Merkel, A., Dobin, A., Lassmann, T., Mortazavi, A., Tanzer, A.,
1218 Lagarde, J., Lin, W., Schlesinger, F., et al. (2012). Landscape of transcription in human
1219 cells. Nature *489*, 101-108. 10.1038/nature11233.
1220 21. Mattick, J.S., Amaral, P.P., Carninci, P., Carpenter, S., Chang, H.Y., Chen, L.L., Chen,
1221 R., Dean, C., Dinger, M.E., Fitzgerald, K.A., et al. (2023). Long non-coding RNAs:
1222 definitions, functions, challenges and recommendations. Nat Rev Mol Cell Biol *24*, 430-
1223 447. 10.1038/s41580-022-00566-8.
1224 22. Sigova, A.A., Mullen, A.C., Molinie, B., Gupta, S., Orlando, D.A., Guenther, M.G.,
1225 Almada, A.E., Lin, C., Sharp, P.A., Giallourakis, C.C., and Young, R.A. (2013).
1226 Divergent transcription of long noncoding RNA/mRNA gene pairs in embryonic stem
1227 cells. Proc Natl Acad Sci U S A *110*, 2876-2881. 10.1073/pnas.1221904110.
1228 23. Seila, A.C., Calabrese, J.M., Levine, S.S., Yeo, G.W., Rahl, P.B., Flynn, R.A., Young,
1229 R.A., and Sharp, P.A. (2008). Divergent transcription from active promoters. Science
1230 *322*, 1849-1851. 10.1126/science.1162253.
1231 24. Core, L.J., Waterfall, J.J., and Lis, J.T. (2008). Nascent RNA sequencing reveals
1232 widespread pausing and divergent initiation at human promoters. Science *322*, 1845-
1233 1848. 10.1126/science.1162228.
1234 25. Preker, P., Nielsen, J., Kammler, S., Lykke-Andersen, S., Christensen, M.S., Mapendano,
1235 C.K., Schierup, M.H., and Jensen, T.H. (2008). RNA exosome depletion reveals
1236 transcription upstream of active human promoters. Science *322*, 1851-1854.
1237 10.1126/science.1164096.
1238 26. He, Y., Vogelstein, B., Velculescu, V.E., Papadopoulos, N., and Kinzler, K.W. (2008).
1239 The antisense transcriptomes of human cells. Science *322*, 1855-1857.
1240 10.1126/science.1163853.
1241 27. Yang, F. (2022). Promoter antisense RNAs: beyond transcription by-products of active
1242 promoters. RNA Biol *19*, 533-540. 10.1080/15476286.2022.2062177.
1243 28. Yang, F., Tanasa, B., Micheletti, R., Ohgi, K.A., Aggarwal, A.K., and Rosenfeld, M.G.
1244 (2021). Shape of promoter antisense RNAs regulates ligand-induced transcription
1245 activation. Nature *595*, 444-449. 10.1038/s41586-021-03589-x.

1246 29. Salta, E., and De Strooper, B. (2017). Noncoding RNAs in neurodegeneration. Nat Rev
1247 Neurosci *18*, 627-640. 10.1038/nrn.2017.90.
1248 30. Idda, M.L., Munk, R., Abdelmohsen, K., and Gorospe, M. (2018). Noncoding RNAs in
1249 Alzheimer's disease. Wiley Interdiscip Rev RNA *9*. 10.1002/wrna.1463.
1250 31. Rybak-Wolf, A., and Plass, M. (2021). RNA Dynamics in Alzheimer's Disease.
1251 Molecules *26*. 10.3390/molecules26175113.
1252 32. Faghihi, M.A., Modarresi, F., Khalil, A.M., Wood, D.E., Sahagan, B.G., Morgan, T.E.,
1253 Finch, C.E., St Laurent, G., 3rd, Kenny, P.J., and Wahlestedt, C. (2008). Expression of a
1254 noncoding RNA is elevated in Alzheimer's disease and drives rapid feed-forward
1255 regulation of beta-secretase. Nat Med *14*, 723-730. 10.1038/nm1784.
1256 33. Simone, R., Javad, F., Emmett, W., Wilkins, O.G., Almeida, F.L., Barahona-Torres, N.,
1257 Zareba-Paslawska, J., Ehteramyan, M., Zuccotti, P., Modelska, A., et al. (2021). MIR-
1258 NATs repress MAPT translation and aid proteostasis in neurodegeneration. Nature *594*,
1259 117-123. 10.1038/s41586-021-03556-6.
1260 34. Policarpo, R., Wolfs, L., Martínez-Montero, S., Vandermeulen, L., Royaux, I., Peer,
1261 G.V., Mestdagh, P., Sierksma, A., Strooper, B.D., and d'Ydewalle, C. (2023). The MIR-
1262 NAT MAPT-AS1 does not regulate Tau expression in human neurons. bioRxiv,
1263 2023.2001.2027.525631. 10.1101/2023.01.27.525631.
1264 35. Jobson, D.D., Hase, Y., Clarkson, A.N., and Kalaria, R.N. (2021). The role of the medial
1265 prefrontal cortex in cognition, ageing and dementia. Brain Commun *3*, fcab125.
1266 10.1093/braincomms/fcab125.
1267 36. Nativio, R., Lan, Y., Donahue, G., Sidoli, S., Berson, A., Srinivasan, A.R.,
1268 Shcherbakova, O., Amlie-Wolf, A., Nie, J., Cui, X., et al. (2020). An integrated multi-
1269 omics approach identifies epigenetic alterations associated with Alzheimer's disease. Nat
1270 Genet *52*, 1024-1035. 10.1038/s41588-020-0696-0.
1271 37. Subramanian, J., Savage, J.C., and Tremblay, M.E. (2020). Synaptic Loss in Alzheimer's
1272 Disease: Mechanistic Insights Provided by Two-Photon in vivo Imaging of Transgenic
1273 Mouse Models. Front Cell Neurosci *14*, 592607. 10.3389/fncel.2020.592607.
1274 38. Mathys, H., Peng, Z., Boix, C.A., Victor, M.B., Leary, N., Babu, S., Abdelhady, G.,
1275 Jiang, X., Ng, A.P., Ghafari, K., et al. (2023). Single-cell atlas reveals correlates of high
1276 cognitive function, dementia, and resilience to Alzheimer's disease pathology. Cell *186*,
1277 4365-4385 e4327. 10.1016/j.cell.2023.08.039.
1278 39. Zhang, Y., Liu, T., Meyer, C.A., Eeckhoute, J., Johnson, D.S., Bernstein, B.E., Nusbaum,
1279 C., Myers, R.M., Brown, M., Li, W., and Liu, X.S. (2008). Model-based analysis of
1280 ChIP-Seq (MACS). Genome Biol *9*, R137. 10.1186/gb-2008-9-9-r137.
1281 40. Xiong, X., Hou, L., Park, Y.P., Molinie, B., Consortium, G.T., Gregory, R.I., and Kellis,
1282 M. (2021). Genetic drivers of m(6)A methylation in human brain, lung, heart and muscle.
1283 Nat Genet *53*, 1156-1165. 10.1038/s41588-021-00890-3.
1284 41. Porman, A.M., Roberts, J.T., Duncan, E.D., Chrupcala, M.L., Levine, A.A., Kennedy,
1285 M.A., Williams, M.M., Richer, J.K., and Johnson, A.M. (2022). A single N6-
1286 methyladenosine site regulates lncRNA HOTAIR function in breast cancer cells. PLoS
1287 Biol *20*, e3001885. 10.1371/journal.pbio.3001885.
1288 42. Schwalb, B., Michel, M., Zacher, B., Fruhauf, K., Demel, C., Tresch, A., Gagneur, J., and
1289 Cramer, P. (2016). TT-seq maps the human transient transcriptome. Science *352*, 1225-
1290 1228. 10.1126/science.aad9841.

1291 43. Shao, R., Kumar, B., Lidschreiber, K., Lidschreiber, M., Cramer, P., and Elsasser, S.J.
1292 (2022). Distinct transcription kinetics of pluripotent cell states. Mol Syst Biol *18*, e10407.
1293 10.15252/msb.202110407.
1294 44. Murakami, S., and Jaffrey, S.R. (2022). Hidden codes in mRNA: Control of gene
1295 expression by m(6)A. Mol Cell *82*, 2236-2251. 10.1016/j.molcel.2022.05.029.
1296 45. Oakley, H., Cole, S.L., Logan, S., Maus, E., Shao, P., Craft, J., Guillozet-Bongaarts, A.,
1297 Ohno, M., Disterhoft, J., Van Eldik, L., et al. (2006). Intraneuronal beta-amyloid
1298 aggregates, neurodegeneration, and neuron loss in transgenic mice with five familial
1299 Alzheimer's disease mutations: potential factors in amyloid plaque formation. J Neurosci
1300 *26*, 10129-10140. 10.1523/JNEUROSCI.1202-06.2006.
1301 46. Oddo, S., Caccamo, A., Shepherd, J.D., Murphy, M.P., Golde, T.E., Kayed, R.,
1302 Metherate, R., Mattson, M.P., Akbari, Y., and LaFerla, F.M. (2003). Triple-transgenic
1303 model of Alzheimer's disease with plaques and tangles: intracellular Abeta and synaptic
1304 dysfunction. Neuron *39*, 409-421. 10.1016/s0896-6273(03)00434-3.
1305 47. Udeochu, J.C., Amin, S., Huang, Y., Fan, L., Torres, E.R.S., Carling, G.K., Liu, B.,
1306 McGurran, H., Coronas-Samano, G., Kauwe, G., et al. (2023). Tau activation of
1307 microglial cGAS-IFN reduces MEF2C-mediated cognitive resilience. Nat Neurosci *26*,
1308 737-750. 10.1038/s41593-023-01315-6.
1309 48. Oblak, A.L., Lin, P.B., Kotredes, K.P., Pandey, R.S., Garceau, D., Williams, H.M., Uyar,
1310 A., O'Rourke, R., O'Rourke, S., Ingraham, C., et al. (2021). Comprehensive Evaluation of
1311 the 5XFAD Mouse Model for Preclinical Testing Applications: A MODEL-AD Study.
1312 Front Aging Neurosci *13*, 713726. 10.3389/fnagi.2021.713726.
1313 49. Lee, A.J., Kim, C., Park, S., Joo, J., Choi, B., Yang, D., Jun, K., Eom, J., Lee, S.J.,
1314 Chung, S.J., et al. (2023). Characterization of altered molecular mechanisms in
1315 Parkinson's disease through cell type-resolved multiomics analyses. Sci Adv *9*, eabo2467.
1316 10.1126/sciadv.abo2467.
1317 50. Conlon, E.G., Fagegaltier, D., Agius, P., Davis-Porada, J., Gregory, J., Hubbard, I., Kang,
1318 K., Kim, D., New York Genome Center, A.L.S.C., Phatnani, H., et al. (2018).
1319 Unexpected similarities between C9ORF72 and sporadic forms of ALS/FTD suggest a
1320 common disease mechanism. Elife *7*. 10.7554/eLife.37754.
1321 51. Tam, O.H., Rozhkov, N.V., Shaw, R., Kim, D., Hubbard, I., Fennessey, S., Propp, N.,
1322 Consortium, N.A., Fagegaltier, D., Harris, B.T., et al. (2019). Postmortem Cortex
1323 Samples Identify Distinct Molecular Subtypes of ALS: Retrotransposon Activation,
1324 Oxidative Stress, and Activated Glia. Cell Rep *29*, 1164-1177 e1165.
1325 10.1016/j.celrep.2019.09.066.
1326 52. Morabito, S., Miyoshi, E., Michael, N., Shahin, S., Martini, A.C., Head, E., Silva, J.,
1327 Leavy, K., Perez-Rosendahl, M., and Swarup, V. (2021). Single-nucleus chromatin
1328 accessibility and transcriptomic characterization of Alzheimer's disease. Nat Genet *53*,
1329 1143-1155. 10.1038/s41588-021-00894-z.
1330 53. Lin, Y.T., Seo, J., Gao, F., Feldman, H.M., Wen, H.L., Penney, J., Cam, H.P., Gjoneska,
1331 E., Raja, W.K., Cheng, J., et al. (2018). APOE4 Causes Widespread Molecular and
1332 Cellular Alterations Associated with Alzheimer's Disease Phenotypes in Human iPSC-
1333 Derived Brain Cell Types. Neuron *98*, 1141-1154 e1147. 10.1016/j.neuron.2018.05.008.
1334 54. Wang, C., Ward, M.E., Chen, R., Liu, K., Tracy, T.E., Chen, X., Xie, M., Sohn, P.D.,
1335 Ludwig, C., Meyer-Franke, A., et al. (2017). Scalable Production of iPSC-Derived

1336 Human Neurons to Identify Tau-Lowering Compounds by High-Content Screening. Stem
1337 Cell Reports *9*, 1221-1233. 10.1016/j.stemcr.2017.08.019.
1338 55. Yankova, E., Blackaby, W., Albertella, M., Rak, J., De Braekeleer, E., Tsagkogeorga, G.,
1339 Pilka, E.S., Aspris, D., Leggate, D., Hendrick, A.G., et al. (2021). Small-molecule
1340 inhibition of METTL3 as a strategy against myeloid leukaemia. Nature *593*, 597-601.
1341 10.1038/s41586-021-03536-w.
1342 56. Yang, R., Feng, X., Arias-Cavieres, A., Mitchell, R.M., Polo, A., Hu, K., Zhong, R., Qi,
1343 C., Zhang, R.S., Westneat, N., et al. (2023). Upregulation of SYNGAP1 expression in
1344 mice and human neurons by redirecting alternative splicing. Neuron *111*, 1637-1650
1345 e1635. 10.1016/j.neuron.2023.02.021.
1346 57. Harrington, A.J., Raissi, A., Rajkovich, K., Berto, S., Kumar, J., Molinaro, G., Raduazzo,
1347 J., Guo, Y., Loerwald, K., Konopka, G., et al. (2016). MEF2C regulates cortical
1348 inhibitory and excitatory synapses and behaviors relevant to neurodevelopmental
1349 disorders. Elife *5*. 10.7554/eLife.20059.
1350 58. Kim, M.S., Akhtar, M.W., Adachi, M., Mahgoub, M., Bassel-Duby, R., Kavalali, E.T.,
1351 Olson, E.N., and Monteggia, L.M. (2012). An essential role for histone deacetylase 4 in
1352 synaptic plasticity and memory formation. J Neurosci *32*, 10879-10886.
1353 10.1523/JNEUROSCI.2089-12.2012.
1354 59. Wen, X., Luo, Z., Zhao, W., Calandrelli, R., Nguyen, T.C., Wan, X., Charles Richard,
1355 J.L., and Zhong, S. (2024). Single-cell multiplex chromatin and RNA interactions in
1356 ageing human brain. Nature *628*, 648-656. 10.1038/s41586-024-07239-w.
1357 60. Barker, S.J., Raju, R.M., Milman, N.E.P., Wang, J., Davila-Velderrain, J., Gunter-
1358 Rahman, F., Parro, C.C., Bozzelli, P.L., Abdurrob, F., Abdelaal, K., et al. (2021). MEF2
1359 is a key regulator of cognitive potential and confers resilience to neurodegeneration. Sci
1360 Transl Med *13*, eabd7695. 10.1126/scitranslmed.abd7695.
1361 61. Targa Dias Anastacio, H., Matosin, N., and Ooi, L. (2022). Neuronal hyperexcitability in
1362 Alzheimer's disease: what are the drivers behind this aberrant phenotype? Transl
1363 Psychiatry *12*, 257. 10.1038/s41398-022-02024-7.
1364 62. Wang, R., and Reddy, P.H. (2017). Role of Glutamate and NMDA Receptors in
1365 Alzheimer's Disease. J Alzheimers Dis *57*, 1041-1048. 10.3233/JAD-160763.
1366 63. Kim, J.H., Lee, H.K., Takamiya, K., and Huganir, R.L. (2003). The role of synaptic
1367 GTPase-activating protein in neuronal development and synaptic plasticity. J Neurosci
1368 *23*, 1119-1124. 10.1523/JNEUROSCI.23-04-01119.2003.
1369 64. Komiyama, N.H., Watabe, A.M., Carlisle, H.J., Porter, K., Charlesworth, P., Monti, J.,
1370 Strathdee, D.J., O'Carroll, C.M., Martin, S.J., Morris, R.G., et al. (2002). SynGAP
1371 regulates ERK/MAPK signaling, synaptic plasticity, and learning in the complex with
1372 postsynaptic density 95 and NMDA receptor. J Neurosci *22*, 9721-9732.
1373 10.1523/JNEUROSCI.22-22-09721.2002.
1374 65. Okamoto, S., Li, Z., Ju, C., Scholzke, M.N., Mathews, E., Cui, J., Salvesen, G.S., Bossy-
1375 Wetzel, E., and Lipton, S.A. (2002). Dominant-interfering forms of MEF2 generated by
1376 caspase cleavage contribute to NMDA-induced neuronal apoptosis. Proc Natl Acad Sci U
1377 S A *99*, 3974-3979. 10.1073/pnas.022036399.
1378 66. Barbosa, A.C., Kim, M.S., Ertunc, M., Adachi, M., Nelson, E.D., McAnally, J.,
1379 Richardson, J.A., Kavalali, E.T., Monteggia, L.M., Bassel-Duby, R., and Olson, E.N.
1380 (2008). MEF2C, a transcription factor that facilitates learning and memory by negative

1381 regulation of synapse numbers and function. Proc Natl Acad Sci U S A *105*, 9391-9396.
1382 10.1073/pnas.0802679105.
1383 67. Fenton, T.A., Haouchine, O.Y., Hallam, E.L., Smith, E.M., Jackson, K.C., Rahbarian, D.,
1384 Canales, C., Adhikari, A., Nord, A.S., Ben-Shalom, R., and Silverman, J.L. (2023).
1385 Hyperexcitability and translational phenotypes in a preclinical model of SYNGAP1
1386 mutations. bioRxiv. 10.1101/2023.07.24.550093.
1387 68. Miyamoto, T., Stein, L., Thomas, R., Djukic, B., Taneja, P., Knox, J., Vossel, K., and
1388 Mucke, L. (2017). Phosphorylation of tau at Y18, but not tau-fyn binding, is required for
1389 tau to modulate NMDA receptor-dependent excitotoxicity in primary neuronal culture.
1390 Mol Neurodegener *12*, 41. 10.1186/s13024-017-0176-x.
1391 69. Talantova, M., Sanz-Blasco, S., Zhang, X., Xia, P., Akhtar, M.W., Okamoto, S.,
1392 Dziewczapolski, G., Nakamura, T., Cao, G., Pratt, A.E., et al. (2013). Abeta induces
1393 astrocytic glutamate release, extrasynaptic NMDA receptor activation, and synaptic loss.
1394 Proc Natl Acad Sci U S A *110*, E2518-2527. 10.1073/pnas.1306832110.
1395 70. Zeng, M., Shang, Y., Araki, Y., Guo, T., Huganir, R.L., and Zhang, M. (2016). Phase
1396 Transition in Postsynaptic Densities Underlies Formation of Synaptic Complexes and
1397 Synaptic Plasticity. Cell *166*, 1163-1175 e1112. 10.1016/j.cell.2016.07.008.
1398 71. Tsai, N.P., Wilkerson, J.R., Guo, W., Maksimova, M.A., DeMartino, G.N., Cowan, C.W.,
1399 and Huber, K.M. (2012). Multiple autism-linked genes mediate synapse elimination via
1400 proteasomal degradation of a synaptic scaffold PSD-95. Cell *151*, 1581-1594.
1401 10.1016/j.cell.2012.11.040.
1402 72. Minkeviciene, R., Rheims, S., Dobszay, M.B., Zilberter, M., Hartikainen, J., Fulop, L.,
1403 Penke, B., Zilberter, Y., Harkany, T., Pitkanen, A., and Tanila, H. (2009). Amyloid beta-
1404 induced neuronal hyperexcitability triggers progressive epilepsy. J Neurosci *29*, 3453-
1405 3462. 10.1523/JNEUROSCI.5215-08.2009.
1406 73. Zott, B., Simon, M.M., Hong, W., Unger, F., Chen-Engerer, H.J., Frosch, M.P.,
1407 Sakmann, B., Walsh, D.M., and Konnerth, A. (2019). A vicious cycle of beta amyloid-
1408 dependent neuronal hyperactivation. Science *365*, 559-565. 10.1126/science.aay0198.
1409 74. Li, Y., Dou, X., Liu, J., Xiao, Y., Zhang, Z., Hayes, L., Wu, R., Fu, X., Ye, Y., Yang, B.,
1410 et al. (2023). Globally reduced N(6)-methyladenosine (m(6)A) in C9ORF72-ALS/FTD
1411 dysregulates RNA metabolism and contributes to neurodegeneration. Nat Neurosci *26*,
1412 1328-1338. 10.1038/s41593-023-01374-9.
1413 75. Congdon, E.E., Ji, C., Tetlow, A.M., Jiang, Y., and Sigurdsson, E.M. (2023). Tau-
1414 targeting therapies for Alzheimer disease: current status and future directions. Nat Rev
1415 Neurol *19*, 715-736. 10.1038/s41582-023-00883-2.
1416 76. Jun, G., Ibrahim-Verbaas, C.A., Vronskaya, M., Lambert, J.C., Chung, J., Naj, A.C.,
1417 Kunkle, B.W., Wang, L.S., Bis, J.C., Bellenguez, C., et al. (2016). A novel Alzheimer
1418 disease locus located near the gene encoding tau protein. Mol Psychiatry *21*, 108-117.
1419 10.1038/mp.2015.23.
1420 77. Bellenguez, C., Kucukali, F., Jansen, I.E., Kleineidam, L., Moreno-Grau, S., Amin, N.,
1421 Naj, A.C., Campos-Martin, R., Grenier-Boley, B., Andrade, V., et al. (2022). New
1422 insights into the genetic etiology of Alzheimer's disease and related dementias. Nat Genet
1423 *54*, 412-436. 10.1038/s41588-022-01024-z.
1424 78. Rodriguez, J., Ren, G., Day, C.R., Zhao, K., Chow, C.C., and Larson, D.R. (2019).
1425 Intrinsic Dynamics of a Human Gene Reveal the Basis of Expression Heterogeneity. Cell
1426 *176*, 213-226 e218. 10.1016/j.cell.2018.11.026.

1427 79. Xu, A., Liu, M., Huang, M.F., Zhang, Y., Hu, R., Gingold, J.A., Liu, Y., Zhu, D., Chien,
1428 C.S., Wang, W.C., et al. (2023). Rewired m(6)A epitranscriptomic networks link mutant
1429 p53 to neoplastic transformation. Nat Commun *14*, 1694. 10.1038/s41467-023-37398-9.
1430 80. McQuade, A., Coburn, M., Tu, C.H., Hasselmann, J., Davtyan, H., and Blurton-Jones, M.
1431 (2018). Development and validation of a simplified method to generate human microglia
1432 from pluripotent stem cells. Mol Neurodegener *13*, 67. 10.1186/s13024-018-0297-x.
1433 81. Brownjohn, P.W., Smith, J., Solanki, R., Lohmann, E., Houlden, H., Hardy, J., Dietmann,
1434 S., and Livesey, F.J. (2018). Functional Studies of Missense TREM2 Mutations in
1435 Human Stem Cell-Derived Microglia. Stem Cell Reports *10*, 1294-1307.
1436 10.1016/j.stemcr.2018.03.003.
1437 82. Zaepfel, B.L., Zhang, Z., Maulding, K., Coyne, A.N., Cheng, W., Hayes, L.R., Lloyd,
1438 T.E., Sun, S., and Rothstein, J.D. (2021). UPF1 reduces C9orf72 HRE-induced
1439 neurotoxicity in the absence of nonsense-mediated decay dysfunction. Cell Rep *34*,
1440 108925. 10.1016/j.celrep.2021.108925.
1441 83. Kim, D., Paggi, J.M., Park, C., Bennett, C., and Salzberg, S.L. (2019). Graph-based
1442 genome alignment and genotyping with HISAT2 and HISAT-genotype. Nat Biotechnol
1443 *37*, 907-915. 10.1038/s41587-019-0201-4.
1444 84. Pertea, M., Pertea, G.M., Antonescu, C.M., Chang, T.C., Mendell, J.T., and Salzberg,
1445 S.L. (2015). StringTie enables improved reconstruction of a transcriptome from RNA-seq
1446 reads. Nat Biotechnol *33*, 290-295. 10.1038/nbt.3122.
1447 85. Love, M.I., Huber, W., and Anders, S. (2014). Moderated estimation of fold change and
1448 dispersion for RNA-seq data with DESeq2. Genome Biol *15*, 550. 10.1186/s13059-014-
1449 0550-8.
1450 86. Langmead, B., and Salzberg, S.L. (2012). Fast gapped-read alignment with Bowtie 2. Nat
1451 Methods *9*, 357-359. 10.1038/nmeth.1923.
1452 87. Zacher, B., Lidschreiber, M., Cramer, P., Gagneur, J., and Tresch, A. (2014). Annotation
1453 of genomics data using bidirectional hidden Markov models unveils variations in Pol II
1454 transcription cycle. Mol Syst Biol *10*, 768. 10.15252/msb.20145654.
1455 88. Li, H. (2018). Minimap2: pairwise alignment for nucleotide sequences. Bioinformatics
1456 *34*, 3094-3100. 10.1093/bioinformatics/bty191.
1457 89. Wyman, D., Balderrama-Gutierrez, G., Reese, F., Jiang, S., Rahmanian, S., Forner, S.,
1458 Matheos, D., Zeng, W., Williams, B., Trout, D., et al. (2020). A technology-agnostic
1459 long-read analysis pipeline for transcriptome discovery and quantification. bioRxiv,
1460 672931. 10.1101/672931.
1461 90. Quinlan, A.R., and Hall, I.M. (2010). BEDTools: a flexible suite of utilities for
1462 comparing genomic features. Bioinformatics *26*, 841-842.
1463 10.1093/bioinformatics/btq033.
1464 91. Yu, G., Wang, L.G., and He, Q.Y. (2015). ChIPseeker: an R/Bioconductor package for
1465 ChIP peak annotation, comparison and visualization. Bioinformatics *31*, 2382-2383.
1466 10.1093/bioinformatics/btv145.
1467 92. Kolberg, L., Raudvere, U., Kuzmin, I., Vilo, J., and Peterson, H. (2020). gprofiler2 -- an
1468 R package for gene list functional enrichment analysis and namespace conversion toolset
1469 g:Profiler. F1000Res *9*. 10.12688/f1000research.24956.2.
1470 93. Hu, B., Zhuang, X.L., Zhou, L., Zhang, G., Cooper, D.N., and Wu, D.D. (2024).
1471 Deciphering the Role of Rapidly Evolving Conserved Elements in Primate Brain

1472 Development and Exploring Their Potential Involvement in Alzheimer's Disease. Mol
1473 Biol Evol *41*. 10.1093/molbev/msae001.
1474 94. Danielski, K. (2023). Guidance on Processing the 10x Genomics Single Cell Gene
1475 Expression Assay. Methods Mol Biol *2584*, 1-28. 10.1007/978-1-0716-2756-3_1.
1476 95. Hao, Y., Stuart, T., Kowalski, M.H., Choudhary, S., Hoffman, P., Hartman, A.,
1477 Srivastava, A., Molla, G., Madad, S., Fernandez-Granda, C., and Satija, R. (2024).
1478 Dictionary learning for integrative, multimodal and scalable single-cell analysis. Nat
1479 Biotechnol *42*, 293-304. 10.1038/s41587-023-01767-y.
1480 96. Heinz, S., Benner, C., Spann, N., Bertolino, E., Lin, Y.C., Laslo, P., Cheng, J.X., Murre,
1481 C., Singh, H., and Glass, C.K. (2010). Simple combinations of lineage-determining
1482 transcription factors prime cis-regulatory elements required for macrophage and B cell
1483 identities. Mol Cell *38*, 576-589. 10.1016/j.molcel.2010.05.004.
1484 97. Hu, B. (2025). MAPT-paRNA in AD. Zenodo. https://doi.org/10.5281/zenodo.15019230.
1485